CM^2 Magazine

第 139 期

南方科技大学海洋磁学中心主编

https://cm2.sustech.edu.cn/

创刊词

海洋是生命的摇篮，是文明的纽带。地球上最早的生命诞生于海洋，海洋里的生命最终进化成了人类，人类的文化融合又通过海洋得以实现。人因海而兴。

人类对海洋的探索从未停止。从远古时代美丽的神话传说，到麦哲伦的全球航行，再到现代对大洋的科学钻探计划，海洋逐渐从人类敬畏崇拜幻想的精神寄托演变成可以开发利用与科学研究的客观存在。其中，上个世纪与太空探索同步发展的大洋科学钻探计划将人类对海洋的认知推向了崭新的纬度：深海（deep sea）与深时（deep time）。大洋钻探计划让人类知道，奔流不息的大海之下，埋藏的却是亿万年的地球历史。它们记录了地球板块的运动，从而使板块构造学说得到证实；它们记录了地球环境的演变，从而让古海洋学方兴未艾。

在探索海洋的悠久历史中，从大航海时代的导航，到大洋钻探计划中不可或缺的磁性地层学，磁学发挥了不可替代的作用。这不是偶然，因为从微观到宏观，磁性是最基本的物理属性之一，可以说，万物皆有磁性。基于课题组的学科背景和对海洋的理解，我们对海洋的探索以磁学为主要手段，海洋磁学中心因此而生。

海洋磁学中心，简称 CM^2，一为其全名“Centre for Marine Magnetism”的缩写，另者恰与爱因斯坦著名的质能方程 $E = MC^2$ 对称，借以表达我们对科学巨匠的敬仰和对科学的不懈追求。

然而科学从来不是单打独斗的产物。我们以磁学为研究海洋的主攻利器，但绝不仅限于磁学。凡与磁学相关的领域均是我们关注的重点。为了跟踪反映国内外地球科学特别是与磁学有关的地球科学领域的最新研究进展，海洋磁学中心特地主办 CM^2 Magazine，以期与各位地球科学工作者相互交流学习、合作共进！

“海洋孕育了生命，联通了世界，促进了发展”。21 世纪是海洋科学的时代，由陆向海，让我们携手迈进中国海洋科学的黄金时代。

目 录

1. 在全球森林化及荒漠化通过调节大气和海洋环流过程影响远程气候变化

翻译人：仲义 zhongy@sustech.edu.cn

Portmann R., Beyerle U., Davin E., et al. ***Global forestation and deforestation affect remote climate via adjusted atmosphere and ocean circulation*** *[J]. Nature Communications, 2022, 13(1), 5569.*

https://doi.org/10.1038/s41467-022-33279-9

摘要：森林可以储存大量的碳并提供重要的生态系统平衡。因此，大规模的植树有时可以被描述为缓解气候变化及其影响的万灵药。最新关于植树造林的优点和缺点争论集中在森林的碳储存潜力和当地或全球热力学影响方面。本文，作者讨论全球范围内的造林和砍伐是如何改变地球的能量平衡，从而影响全球大气环流及对海洋环流产生深远的影响。作者利用多世纪耦合气候模型模拟，其中工业化前的植被覆盖要么完全被森林覆盖，要么被森林砍伐，使二氧化碳混合比保持恒定。研究表明，全球范围内的森林造林导致了北半球中纬度大气环流的减弱并向极地移动，减缓了大西洋径向翻转流，并影响了哈德莱环流的强度，反之亦然。结果来看，陆地表面的这两种变化对全球区域降水、温度、云层和地面风场模式都有很大的影响。因此，大规模造林项目的设计过程需要充分考虑全球环流调节及其对气候的影响作用。

ABSTRACT: Forests can store large amounts of carbon and provide essential ecosystem services. Massive tree planting is thus sometimes portrayed as a panacea to mitigate climate change and related impacts. Recent controversies about the potential benefits and drawbacks of forestation have centered on the carbon storage potential of forests and the local or global thermodynamic impacts. Here we discuss how global-scale forestation and deforestation change the Earth's energy balance, thereby affect the global atmospheric circulation and even have profound effects on the ocean circulation. We perform multi-century coupled climate model simulations in which preindustrial vegetation cover is either completely forested or deforested and carbon dioxide mixing ratio is kept constant. We show that global-scale forestation leads to a weakening and poleward shift of the

Northern mid-latitude circulation, slows-down the Atlantic meridional overturning circulation, and affects the strength of the Hadley cell, whereas deforestation leads to reversed changes. Consequently, both land surface changes substantially affect regional precipitation, temperature, clouds, and surface wind patterns across the globe. The design process of large-scale forestation projects thus needs to take into account global circulation adjustments and their influence on remote climate.

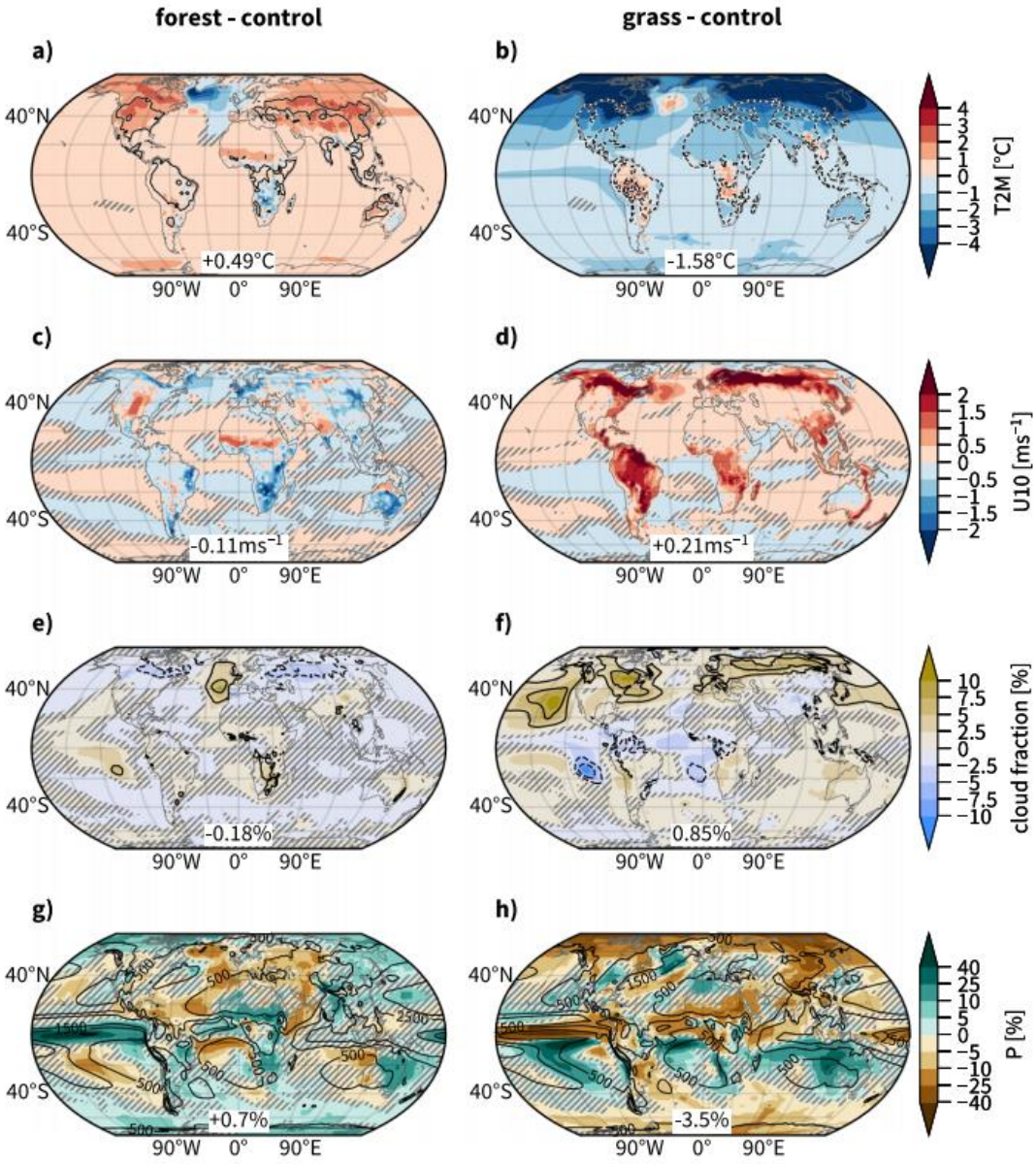

Figure 1. Changes of variables relevant to near-surface weather and climate. Panels (a, c, e, g) show changes in forestand b, d, f, h changes in grass compared to control. Variables shown are (a, b) absolute changes of annual mean 2 m temperature (T2M, shading, in °C) and the number of days with a maximum temperature above 30 °C (heat days, +15 days in solid contours and −15 days dashed) and c, d absolute changes of annual mean 10 m wind speed (shading, in ms−1), e, f absolute changes of annual mean total cloud fractions (shading, in %) and low cloud fractions (black contours, shown are −10, −5, 5, and 10% contour levels), and g, h relative changes in annual mean precipitation (shading, in %, note the nonlinear color spacing). Statistically insignificant results are hatched, see Methods section. This Figure was produced using Cartopy, which is licensed under the GNULesserGeneralPublicLicense.

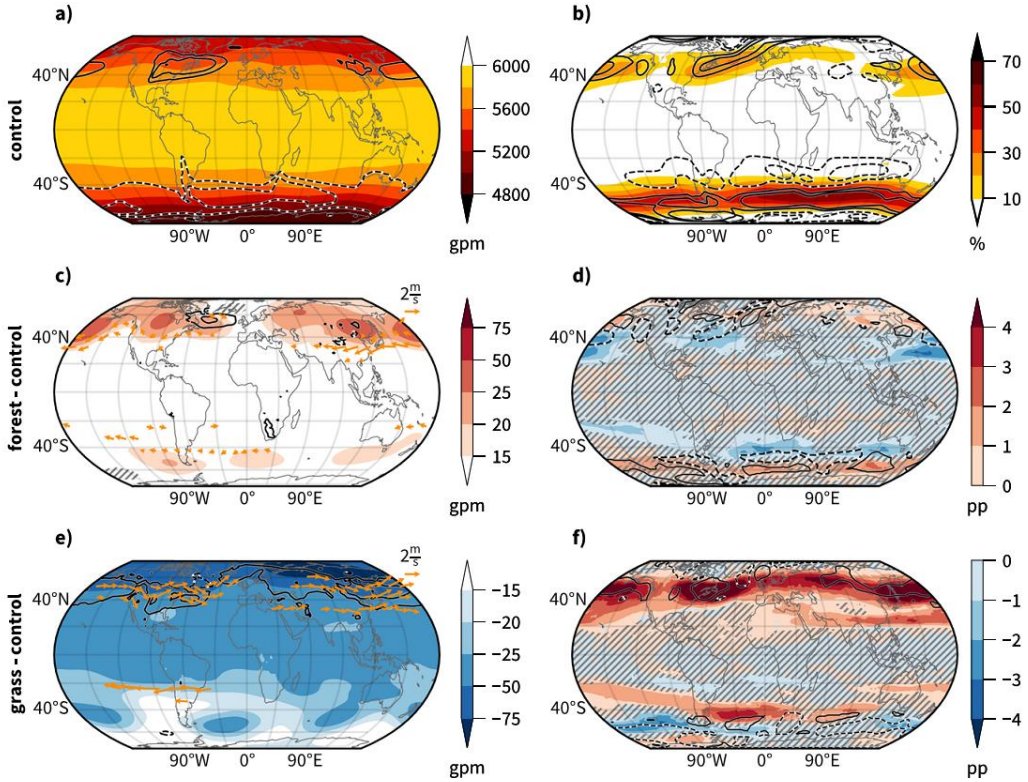

Figure 2. Changes in the extratropical atmospheric circulation. a Annual mean geopotential height at 500hPa (Z500, shading, in gpm)and meridional component of the eddy heat flux at 850hPa (v 0T0, contours, −15, −10, 10, and 15Kms^{-1}) in simulation control, b annual mean frequencies of deep jets (shading, in %) and E-vector divergence (contours, −3, −1.5,1.5 and 3 m^2 s^{-2}(100km^{-1}), c, e differences in annual mean Z500 (shading, in gpm), eddy heat flux at 850hPa (contours, −3, −1, 1, and 3 Kms^{-1}),and representative wind differences at 300hPa (arrows, only the sixty globally largest differences at every tenth latitude and longitude index are shown, i.e., if larger than 0.6ms−1 for forest and 0.6 ms−1 1.4ms−1 int grass) for c forest minus control and e grass minus control, and d, fdifferences of annual mean deep jet frequencies (shading, in percent points [pp]) and E-vector divergence (contours, −0.15 and 0.15m2 s−2(100km)−1, only shown for regions where E-vector divergence is larger than 0.5m2 s−2(100km)−1 in control) for d forest minus control and f grass minus control. For all contours, positive values are solid and negative values dashed. Statistically insignificant changes (see methods) are hatched for variables shown in shading. For other variables, only statistically significant results are shown, except for the changes in E-vector divergence. These fields would otherwise be too patchy in grass and are not significant in forest according to the test used in this study. This Figure was produced using Cartopy, which is licensed under the GNULesserGeneralPublicLicense.

2. 赤铁矿年代学揭示构造驱动的铁矿床形成

翻译人：蒋晓东 jiangxd@sustech.edu.cn

Courtney-Davies L., Danišik M., Ramanaidou E R., et al. ***Hematite geochronology reveals a tectonic trigger for iron ore mineralization during Nuna breakup*** *[J]. Geology 2022, 50, 1318-1323.*

https://doi.org/10.1130/G50374.1

摘要：在西澳大利亚皮尔巴拉的条带状铁建造（BIF）中赋存着赤铁矿和针铁矿矿床，是地球上最重要的铁储量之一。然而，矿床成因的时间和构造触发因素仍存在争议。由于缺乏直接的年龄测量，矿床成因仍然存在不确定性，而理解年代学有助于进行对比 BIF 成矿期与其他地区观测到的构造-热事件。在太古代-古元古代哈默斯利省的 BIF 中含有广泛的假象赤铁矿，间接约束条件显示矿体形成于 2.2～2.0 Ga。相比之下，结合赤铁矿原位 U-Pb 年代学和 (U-Th)/He 年代学证明了奇切斯特地区的假象赤铁矿-微板赤铁矿石形成约为 1.26-1.22 Ga，并在约 0.57～0.38 Ga 之间发生克拉通剥蚀。纳米尺度成像结果指示 U-Th-Pb 为晶格束缚体，未赋存于包裹体中。新 U-Pb 赤铁矿的年龄与在皮尔巴拉和皮尔巴拉的边缘报告的其他矿物年龄重叠，克拉通（1.3～1.1 Ga）受板块重组驱动形成努纳超大陆解体之后。这种年龄相关性表明，超大陆重构造成的造山（+成岩）和热（+流体）生成过程是皮尔巴拉克拉通铁矿形成的关键触发因素。

ABSTRACT: Hematite and goethite deposits hosted in banded iron formations (BIFs) in the Pilbara craton (Western Australia) represent one of Earth's most significant Fe reserves; however, the timing and tectonic triggers underpinning deposit genesis remain contentious. Uncertainty in ore genesis stems from a lack of direct age measurements, which could aid in correlating periods of BIF mineralization with tectono-thermal events observed elsewhere. Archean– Paleoproterozoic BIFs in the Hamersley Province host extensive martite–microplaty hematite orebodies that formed at 2.2–

2.0 Ga, based on indirect constraints. In contrast, combined hematite in situ U-Pb geochronology and (U-Th)/He thermochronology demonstrate that martite–microplaty hematite ores in the Chichester Range crystallized ca. 1.26–1.22 Ga and underwent cratonic denudation between ca. 0.57 and 0.38 Ga. Nanoscale imaging of dated hematite indicates that U-Th-Pb is lattice bound and not hosted in inclusions. New U-Pb hematite ages overlap with other mineral ages reported at the margins of the Pilbara and Yilgarn cratons (1.3–1.1 Ga), where mineral formation was driven by plate reorganization following breakup of the Nuna supercontinent. This age correlation suggests that a combination of increased orogenic (+diagenetic) and heat (+fluid) generative processes resulting from supercontinent reconfiguration was a key trigger for iron ore formation in the Pilbara craton.

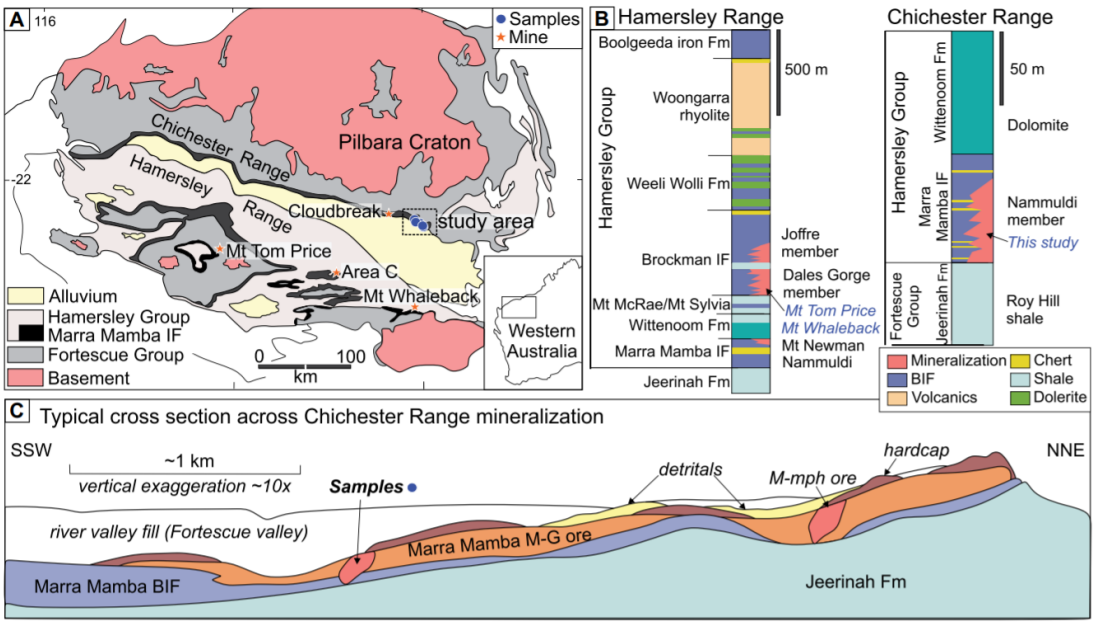

Figure 1. (A) Geologic map of the Pilbara craton (Western Australia) showing sample locations. IF—iron formation. (B) Stratigraphic column depicting the Hamersley Range and Chichester Range, displaying lithologies in which major deposits and studied samples are hosted (modified after Hannon et al., 2005). BIF-banded iron formation. (C) Diagrammatic cross section through deposits in the Nammuldi Member of the Marra Mamba Iron Formation in the Chichester Range, Western Australia (modified after Morris and Kneeshaw, 2011). M-mphmartite–microplaty hematite; M-G—martite-goethite.

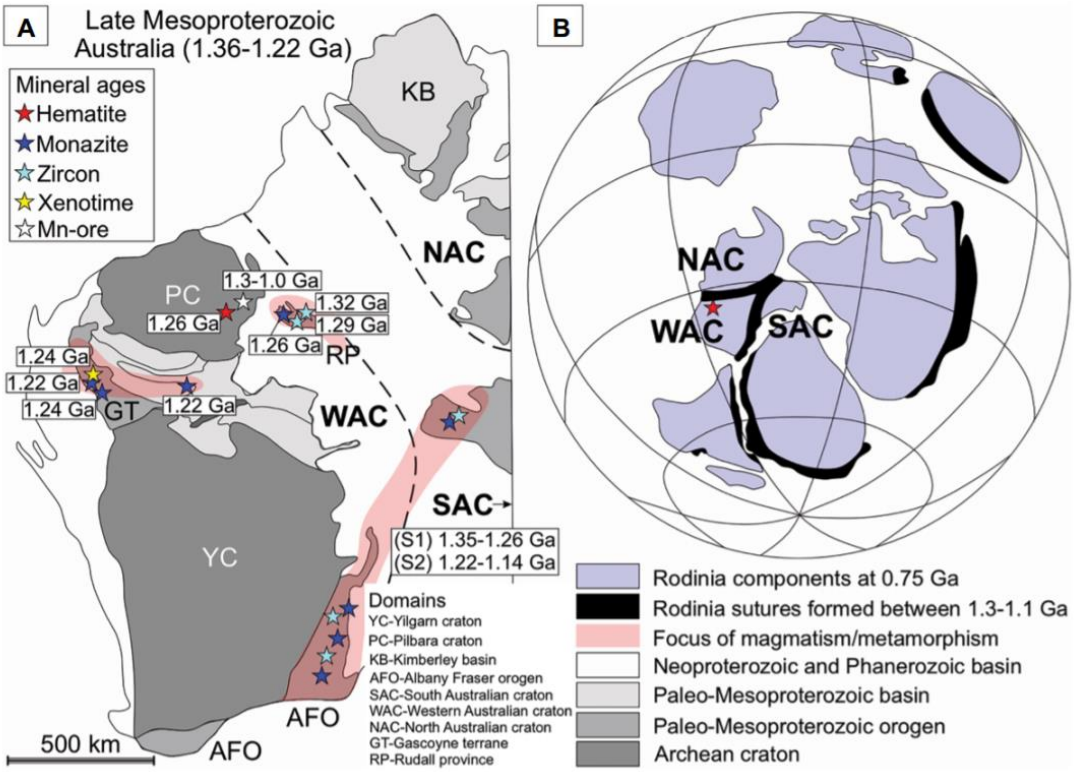

Figure 2. (A) Tectonism and magmatism at 1.36–1.22 Ga in westerncentral Australia (current geographic positions are overlaid). Location of dated hematite is marked and compared with mineral dating from several other studies at the craton margins. (B) Projection showing the main components of Rodinia sutured by orogenic activity between 1.3 and 1.1 Ga (modified after Myers et al., 1996; Cawood and Korsch, 2008).

3. 西班牙北部的 8.2 ka 事件：多指标石笋记录的时间、结构及气候影响

翻译人：盖聪聪 gaicc@sustech.edu.cn

Kilhavn H., Couchoud I., Drysdale R N., et al. ***The 8.2 ka event in northern Spain: timing, structure and climatic impact from a multi-proxy speleothem record*** *[J]. Climate of the Past, 2022, 18, 2321-2344.*

https://doi.org/10.5194/cp-18-2321-2022

摘要：8.2 ka 事件是全新世最突出的气候异常。通常认为该事件由北大西洋的融水释放引发，其规模足以破坏大西洋经向翻转流（AMOC）。格陵兰冰芯捕捉了了最清楚的 8.2 ka 记录，表现为从 8.25±0.05 到 8.09±0.05 ka、持续约 160 年的、寒冷干燥的异常现象。北大西洋地区也记录了 8.2 ka 事件，然而，关于事件时间、演变和影响的解释具有显著差异。这种不一致通常归因于年代框架的不精确和/或时间序列分辨率不够。西班牙北部适合研究 AMOC 扰动对西南欧的影响，本文展示了该区 El Soplao 洞穴早全新世古气候的高分辨率石笋记录。通过耦合石笋稳定碳氧同位素、微量元素（Mg/Ca 和 Sr/Ca）和生长速率等指标，本文在年代际尺度上探索了 8.2 ka 事件的时间和影响。石笋的$\delta^{18}O$ 变化与有效补给有关，这得到了$\delta^{13}C$、Mg/Ca 和生长速率变化的支持。El Soplao 石笋记录的 8.2 ka 事件表现为$\delta^{18}O$ 百年尺度上的负偏移，从 8.19±0.06 ka 持续到 8.05±0.05 ka，表明当时补给增加。尽管这得到了其他指标的支持，但$\delta^{18}O$ 的变化幅度很小，在很大程度上在过去 1000 年的可变范围内。此外，向$\delta^{18}O$ 负偏的时间要早于其他指标的变化时间，本文认为这与北大西洋融水通量相关的水分源同位素组成变化的有关。与欧洲西南部其他定年良好的记录对比，结果表明 8.2 ka 事件的时间是同步的，误差加权后的平均开始时间为 8.23±0.03 ka，结束时间为 8.10±0.05 ka。这与 NGRIP 记录一致。此外，El Soplao 石笋$\delta^{18}O$ 记录与西南部欧洲的其他指标及 NGRIP 冰芯记录在结构上具有相似性。

ABSTRACT: The 8.2 ka event is regarded as the most prominent climate anomaly of the Holocene and is thought to have been triggered by a meltwater release to the North Atlantic that was of

sufficient magnitude to disrupt the Atlantic Meridional Overturning Circulation (AMOC). It is most clearly captured in Greenland ice-core records, where it is reported as a cold and dry anomaly lasting ~160 years, from 8.25 ± 0.05 until 8.09 ± 0.05 ka . It is also recorded in several archives in the North Atlantic region; however, its interpreted timing, evolution and impacts vary significantly. This inconsistency is commonly attributed to poorly constrained chronologies and/or inadequately resolved time series. Here we present a high-resolution speleothem record of early Holocene palaeoclimate from El Soplao Cave in northern Spain, a region pertinent to studying the impacts of AMOC perturbations on south-western Europe. We explore the timing and impact of the 8.2 ka event on a decadal scale by coupling speleothem stable carbon and oxygen isotopic ratios, trace element ratios (Mg/Ca and Sr/Ca), and growth rate. Throughout the entire speleothem record, $\delta^{18}O$ variability is related to changes in effective recharge. This is supported by the pattern of changes in $\delta^{13}C$, Mg/Ca and growth rate. The 8.2 ka event is marked as a centennial-scale negative excursion in El Soplao $\delta^{18}O$, starting at 8.19 ± 0.06 ka and lasting until 8.05 ± 0.05 ka, suggesting increased recharge at the time. Although this is supported by the other proxies, the amplitude of the changes is minor and largely within the realm of variability over the preceding 1000 years. Further, the shift to lower $\delta^{18}O$ leads the other proxies, which we interpret as the imprint of the change in the isotopic composition of the moisture source, associated with the meltwater flux to the North Atlantic. A comparison with other well-dated records from south-western Europe reveals that the timing of the 8.2 ka event was synchronous, with an error-weighted mean age for the onset of 8.23 ± 0.03 and 8.10 ± 0.05 ka for the end of the event. This compares favourably with the North Greenland Ice Core Project (NGRIP) record. The comparison also reveals that the El Soplao $\delta^{18}O$ is structurally similar to the other archives in south-western Europe and the NGRIP ice-core record.

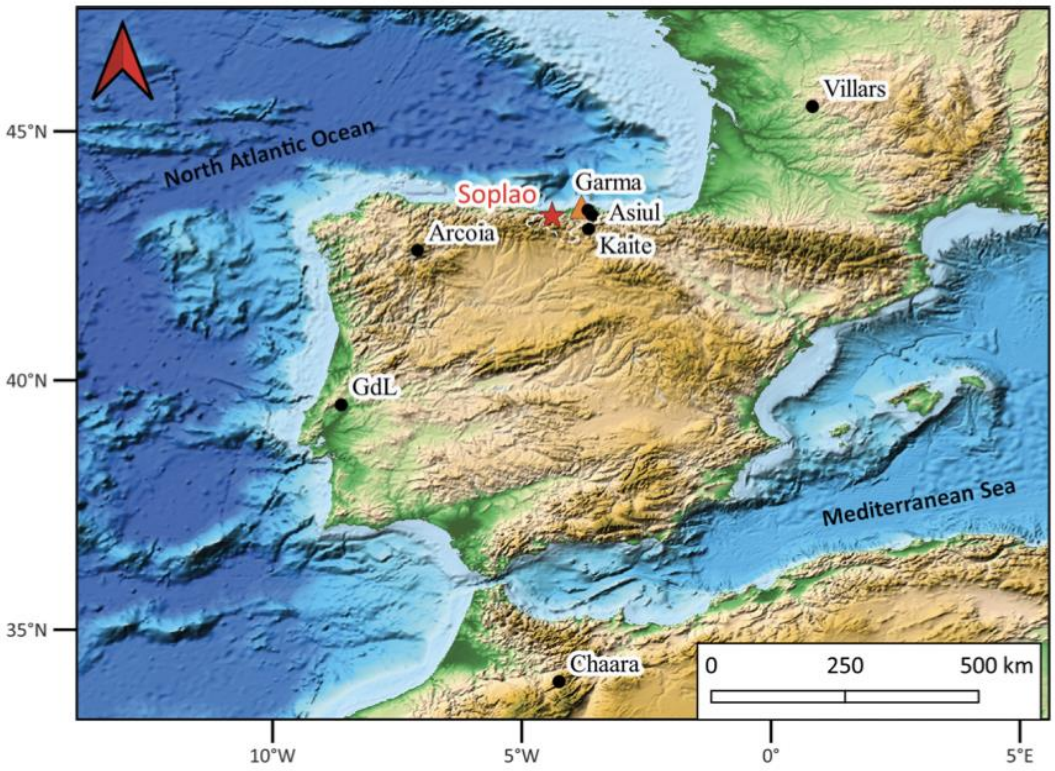

Figure 1. Location of the main palaeoclimate records discussed in the text: Soplao (El Soplao Cave; this study), Garma (La Garma Cave; Baldini et al., 2019), Kaite (Kaite Cave; Domínguez-Villar et al., 2009, 2017), GdL (Galeria das Lâminas; Benson et al., 2021), Chaara (Chaara Cave; Ait Brahim et al., 2019), Asiul (Cueva de Asiul; Smith et al., 2016), Arcoia (Cova da Arcoia; Railsback et al., 2011) and Villars (Villars Cave; Ruan, 2016). Location of the Santander GNIP station is indicated by an orange triangle. Meteorological data from the Cantabrian province (Rodríguez-Arévalo et al., 2011) are measured at various sites located between 42–43°N and 2–6°W (white, stapled line). Base map (ETOPO1 1 Arc-Minute Global Relief Model) collected from NOAA National Geophysical Data Center (2009) and map created in QGIS.

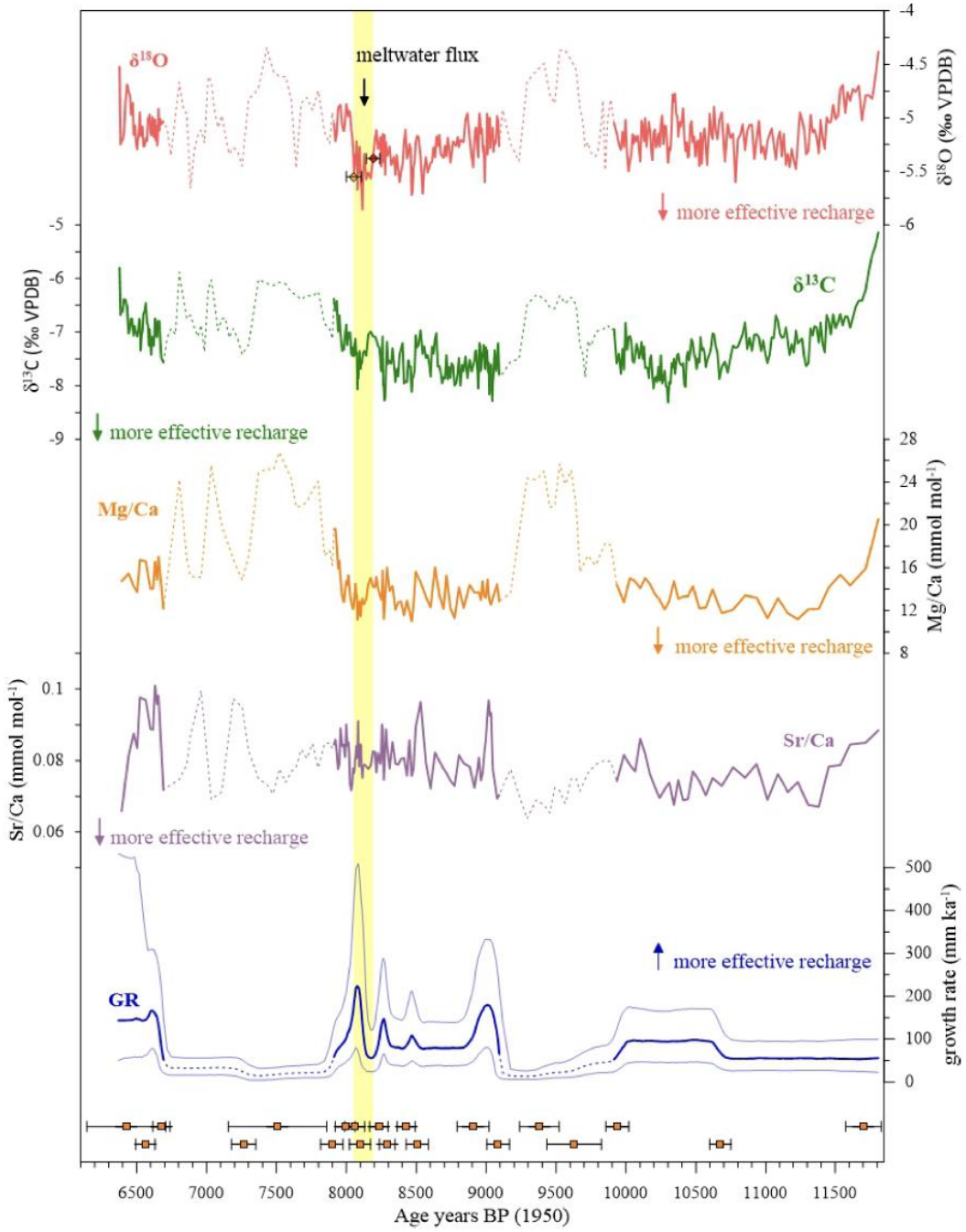

Figure 2. SIR-14 proxy time series. From top: $\delta^{18}O$, $\delta^{13}C$, Mg/Ca, Sr/Ca, growth rate and U–Th dates (2σ uncertainties). The likely position and duration of the 8.2 ka event are determined from the excursion in the $\delta^{18}O$ signal indicated by the yellow shading. The two intervals of relatively low growth rates (GRs < 50 mm kyr^{-1}) are indicated by dotted lines. The variability through these intervals is interpreted to be related to effects specific to the drip site and unrelated to regional climate changes. The growth-rate uncertainties (1σ) are plotted as light blue lines and are derived from the uncertainties in the age model.

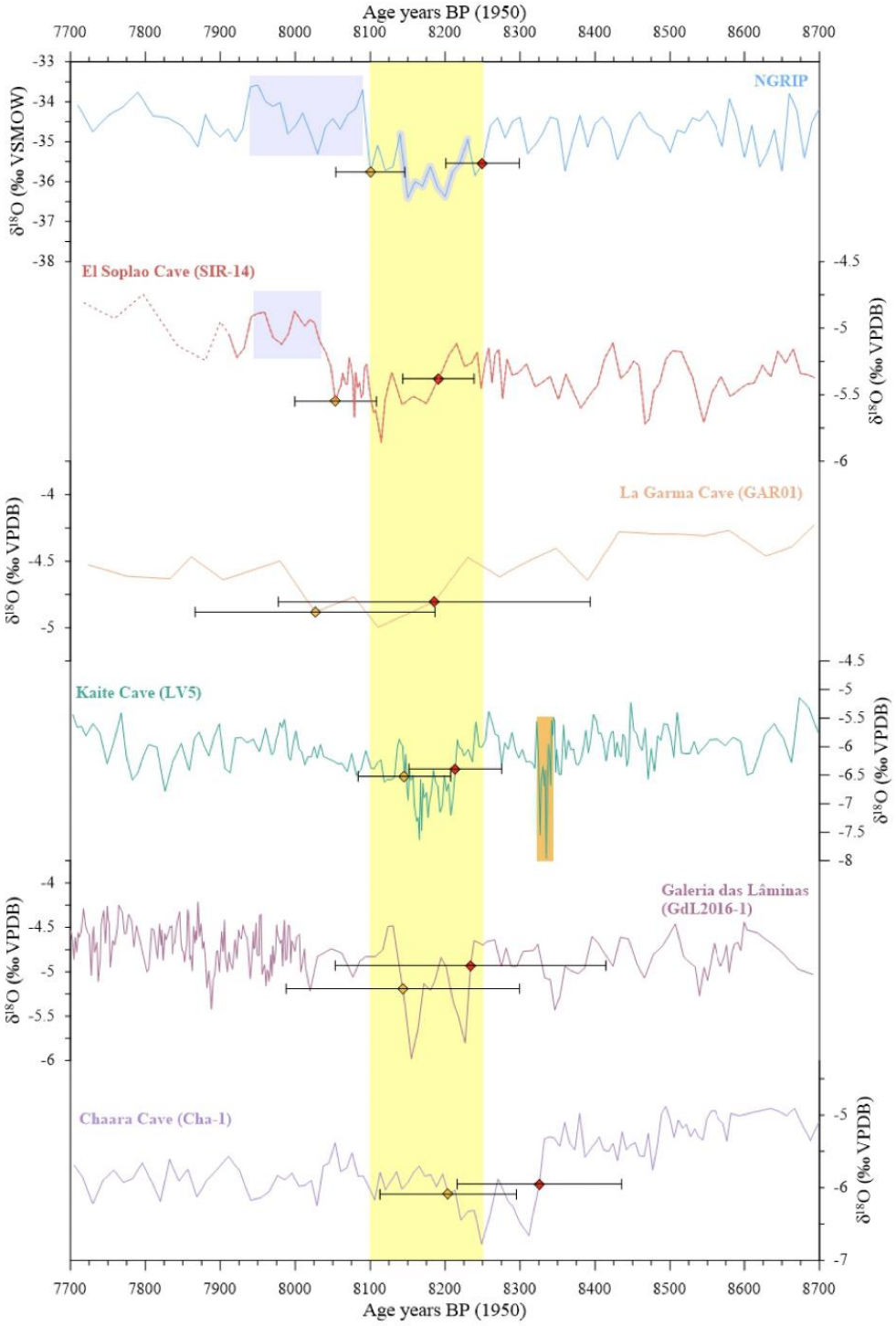

Figure 3. Comparison of $\delta^{18}O$ variability from selected archives across the 8.2 ka event. From top: NGRIP, SIR-14, GAR01, LV5, GdL2016-1 and Cha-1. The duration of the 8.2 ka event (as inferred from the NGRIP record) is highlighted by yellow shading. The double trough (central part of the event; Thomas et al., 2007) is marked with a thick grey line in the NGRIP profile. Orange shading indicates the "precursor event" identified in the Kaite Cave record. Blue shading indicates the interval where $\delta^{18}O$ overshoots after the event in the NGRIP and SIR-14 records.

4. 火星古老沉积盆地河流脊地貌

翻译人：张琪 zhangq7@sustech.edu.cn

Cardenas B., Lamb M., Grotzinger J. ***Martian landscapes of fluvial ridges carved from ancient sedimentary basin fill*** *[J]. Nature Geoscience, 2022.*

https://doi.org/10.1038/s41561-022-01058-2

摘要：大型沉积盆地蕴含着记录地球历史的档案。目前火星上是否存在类似的盆地仍然未知，主要因为缺乏地下观测，且很难对埋藏在地下的沉积物进行确认。本文中，作者用数值模拟的方法展示了火星表面丰富的地形脊网络景观，可能代表一些侵蚀窗口，由此能够进入到长期积累的厚实的河流沉积物。作者使用数值模型来驱动山坡蠕变和来自风的差异侵蚀，用来模拟作用于河流冲积盆地地层的类似火星的挖掘过程，这些地层是埋藏在地球墨西哥湾的地层基于三维反射地震学成像形成的。模拟结果得到清晰的火星地貌，其中泥岩相对于砂岩通道带的优先侵蚀导致了交叉山脊的复杂模式。作者的发现与现有的观点形成对比，后者认为脊状火星景观是一层薄薄的表面沉积物，保存了某个时间点的河流景观。相反，该模式得出的山脊横切图案反映了不同地层层面的河道体，暴露出 50 万年时间尺度积累的盆地地层。因此，作者提出火星上的河流脊可能记录着长期的水环境过程。

ABSTRACT: Large sedimentary basins contain archives of Earth history. It is unknown to what extent similar basins existed on Mars because there are few observations relating to the subsurface and it is difficult to identify buried deposits. Here, we used numerical simulations to show that landscapes of networks of topographic ridges that are abundant on the surface of Mars may represent erosional windows into thick, basin-filling river deposits that accumulated over long-time spans. We used a numerical model to drive hillslope creep and differential erosion from the wind to simulate Mars-like exhumation processes acting on basin-filling fluvial strata, which we based on those buried in the Gulf of Mexico on Earth, as imaged using three-dimensional reflectance seismology. Simulations produced remarkably Martian landscapes in which the preferential erosion of mudstone relative to sandstone channel belts leads to the development of complex patterns of

intersecting ridges. Our findings contrast to the existing view of ridged Martian landscapes as thin-skinned surface deposits preserving fluvial landscapes at a snapshot in time. Instead, the ridge cross-cutting patterns produced by the model reflect the exhumation of channel bodies at different stratigraphic levels, exposing basin strata accumulated over time scales of 500,000 years. Thus, we propose that fluvial ridges on Mars may expose an archive of long-lived aqueous processes.

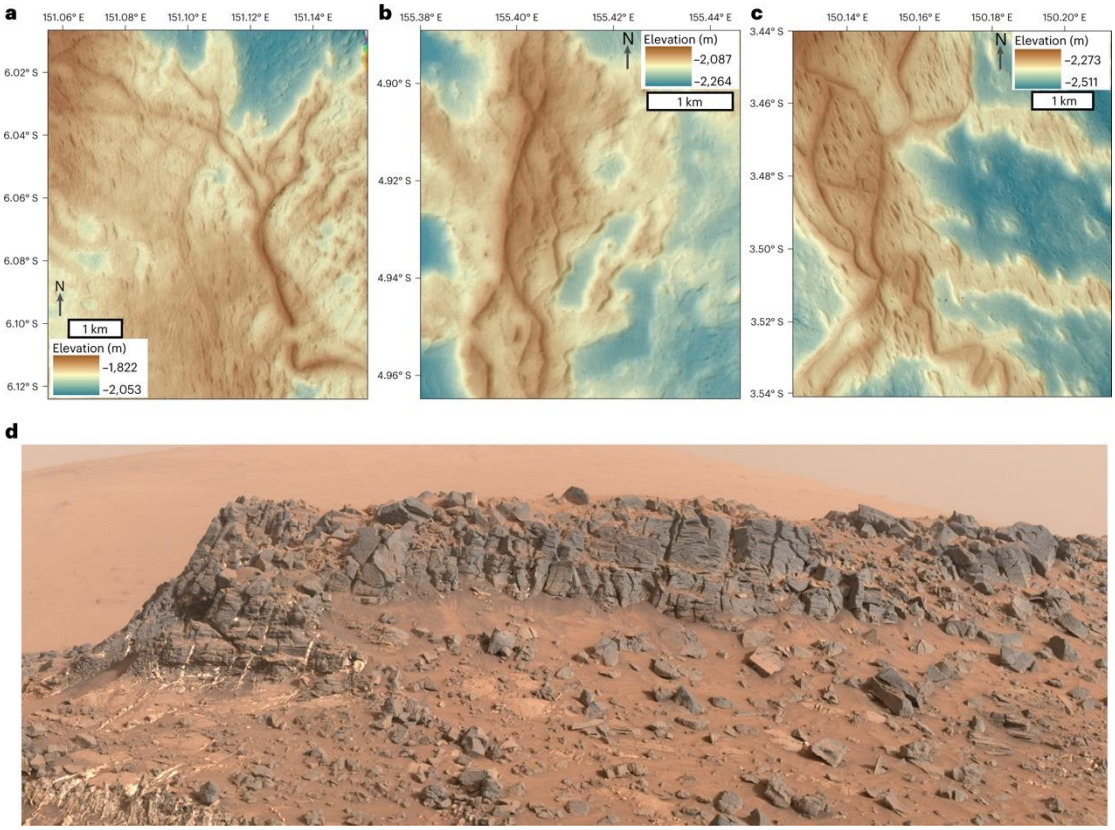

Figure 1. a-c, Digital elevation models constructed from Context Camera stereo pairs of fluvial ridges forming complex intersecting patterns exposed at Aeolis Dorsa (see Supplementary Table 2 for a list of stereo pairs): north-branching network of fluvial ridges (a), network of fluvial ridges branching to the north and south (b) and network of fluvial ridges with complex intersections (c). d, Curiosity rover Mastcam mosaic (ML_4119, sol 938) showing sandstone cliff overlying a sloping exposure of mudstones in the Murray Formation. While this deposit is thought to be subaqueous in origin rather than a fluvial ridge, it illustrates from the ground how differential erosion from the wind has led to cliff-forming sandstones that overlie slope-forming mudstones. The tip of the sandstone exposure is about 1 m thick (image credit for a-d: NASA/JPL-Caltech/MSSS).

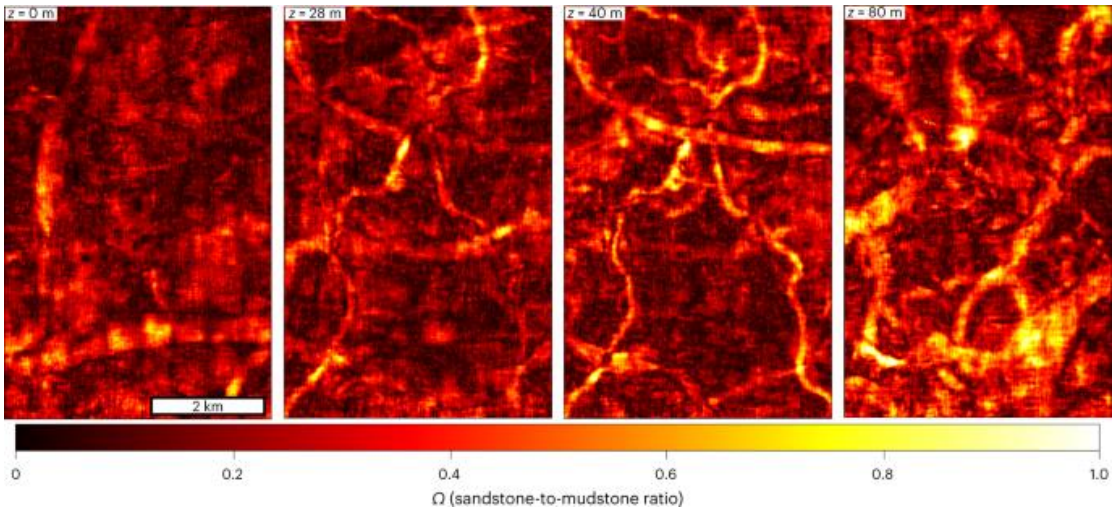

Figure 2. Horizontal slices showing river channel belts in the 3D seismic volume.

5. 雅鲁藏布江流域盆地 Li 同位素的时空变化：来源和过程

翻译人：张靖宇 zhangjy6@sustech.edu.cn

Zhang J W., Yan Y N., Zhao Z Q., et al. ***Spatiotemporal variation of Li isotopes in the Yarlung Tsangpo River basin (upper reaches of the Brahmaputra River): Source and process*** *[J]. Earth and Planetary Science Letters, 2022, 600, 117875.*

https://doi.org/10.1016/j.epsl.2022.117875

摘要：自新生代以来，海洋 Li 同位素组成（δ^7Li，~9‰）的增加可能与构造隆起有关的大陆化学风化有关（如青藏高原）。然而，流经青藏高原的河流中 δ^7Li 的时空变化原因仍有争议，阻碍了对海水 δ^7Li 变化的理解。在此，我们分析了来自雅鲁藏布江流域（青藏高原最大的河流系统）的各种地质样本，即河水、河流悬浮颗粒物、河流沉积物、热泉和硅酸盐岩，以了解流经高海拔和构造地区的河流中溶解性 Li 的来源和同位素分馏。与大多数河流水体相比，雅鲁藏布江的溶解 Li 浓度（$[Li]_{dis}$）异常高（0.5-313μg/L，平均 58.4μg/L，n=93），δ^7Li_{dis} 值较低（+1.0‰-+14.7‰，平均+6.4‰，n=92）。这些结果可以解释为地下热水的输入具有极高的$[Li]_{dis}$（5.5-34.4 mg/L，平均 15.7 mg/L，n=9）和低的 δ^7Li_{dis}（-1.7‰-+3.1‰，平均+1.0‰）。与地下热水相比，硅酸盐风化可能是河水中 δ^7Li_{dis} 升高的原因，但硅酸盐风化和地下热水的二元混合模型结果并不支持这一猜测。有人认为，正在进行的溶解负荷和次生矿物之间的 Li 同位素分馏是河水中 δ^7Li_{dis} 增加的主要原因。野外研究和吸附实验结果支持河流中持续的 Li 同位素分馏的观点。物理侵蚀和化学风化过程为河流提供新鲜次生矿物，以及来自地下热水的溶解 Li 在河流中停留长时间，促进了 Li 同位素分化。因此，随着大陆地热系统的出现，构造活动可能直接或间接地诱发最终流入海洋的河流中溶解的 Li 通量和 δ^7Li_{dis} 同时增加。这可以解释晚新生代的海水 δ^7Li 的增加。

ABSTRACT: The increase in marine Li isotope composition (δ^7Li, ~9‰) since the Cenozoic is possibly related to continental chemical weathering associated with tectonic uplift (e.g., the Tibetan Plateau [TP]). However, the reasons for the spatiotemporal variations of δ^7Li in the rivers flowing through the TP are still under debate, hindering the understanding of the changes in seawater δ^7Li.

Herein, various geological samples, i.e. river waters, river suspended particulate materials, river sediments, hot springs and silicate rocks, from the Yarlung Tsangpo River basin, the largest river system in the TP, have been analyzed to understand the source and isotopic fractionation of dissolved Li in rivers flowing through high-altitude and tectonic regions. The Yarlung Tsangpo River has an unusually high dissolved Li concentration ($[Li]_{dis}$) (0.5–313 μg/L, mean 58.4 μg/L, n=93) and low δ^7Li_{dis} values (+1.0‰–+14.7‰, mean +6.4‰, n=92) compared with most river waters. These results can be explained by the input of geothermal water with extremely high $[Li]_{dis}$ (5.5–34.4 mg/L, mean 15.7 mg/L, n=9) and low δ^7Li_{dis} (−1.7‰–+3.1‰, mean +1.0‰). Silicate weathering is probably responsible for elevated δ^7Li_{dis} in river water compared to geothermal water, but the binary mixture model results of silicate weathering and geothermal water do not support this speculation. Ongoing Li isotope fractionation between dissolved loads and secondary minerals has been suggested to be the main reason for the increased δ^7Li_{dis} in river water. Field study and adsorption experiment results support the view of continuous Li isotope fractionation in rivers. Physical erosion and chemical weathering processes that provide fresh secondary minerals to rivers as well as dissolved Li from geothermal water transported in rivers over long residence times promote Li isotope fractionation. Hence, with the emergence of a continental geothermal system, the tectonic activity may directly or indirectly induce the simultaneous increase in dissolved Li flux and δ^7Li_{dis} in rivers that eventually flow into the ocean. This can partially explain the increase in seawater δ^7Li in the Late Cenozoic.

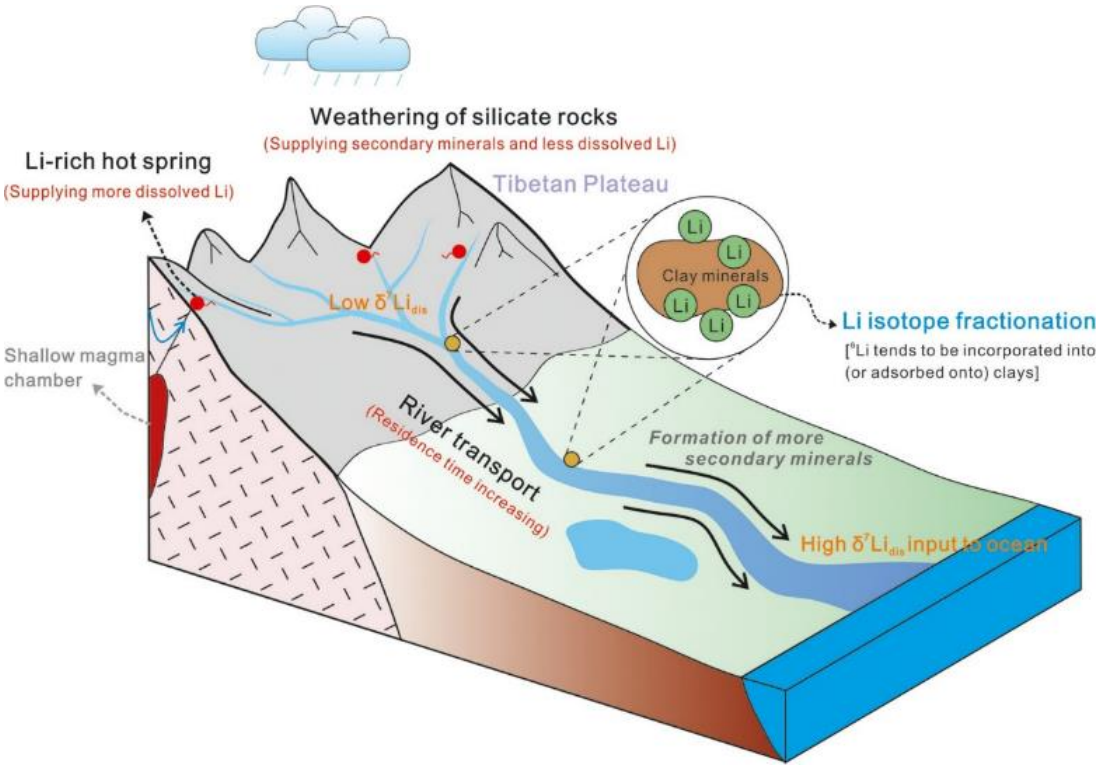

Figure 1. A conceptual model for the source and fractionation of dissolved Li in rivers originated from the TP.

6. 通过伸展和高热流作用导致的南海大陆裂陷

翻译人：刘伟 inewway@163.com

Burton-Johnson A., Cullen A B. ***Continental rifting in the South China Sea through extension and high heat flow: An extended history*** *[J]. Gondwana Research, 2022.*

https://doi.org/10.1016/j.gr.2022.07.015

摘要：本文提出了一种新的伸展构造模型，描述了新生代东南亚和南海打开的历史，提出了陆内裂陷在不引起地幔柱的情况下启动和传播的反馈机制。提出了南海打开的四种主要构造模式：1)古南海俯冲的板片拖曳；2)印亚碰撞导致的挤出构造；3)地幔柱作用；4)弧后裂陷作用。每个模型都是围绕不同的特定数据开发的，并且都倾向于通过选择性的数据优先级而自恰。我们提出了一个新的 GPlates 模型，表明南海共轭边缘之间的地质和地球物理特征与华南边缘相吻合，中生代以来的区域伸展也与婆罗洲已有的古地磁资料吻合。东南亚岩石圈长期伸展的地球动力学机制是通过传递式反馈过程发展的，由中生代板块回滚和华南俯冲带的迁移开始，导致陆内减薄和伸展。这反过来又驱动了被动的软流圈上升，增加了热流和地壳延展性，并进一步增强了作为一个宽裂谷而不是窄的地壳颈的发展。随后，随着大陆的充分延伸，南海洋壳开始出现并扩张。这种反馈机制(涉及浅地幔过程，而不是深地幔过程)可能会增强和促进其他地方的大陆裂陷作用。

ABSTRACT: We present a new extensional tectonic model for the Cenozoic history of SE Asia and the opening of the South China Sea (SCS), proposing a feedback mechanism by which intracontinental rifts initiate and propagate without invoking mantle plumes.Four principal tectonic models have been proposed for SCS opening: 1) Slab pull from subduction of a Proto South China Sea (PSCS); 2) Extrusion tectonics from the India-Asia collision; 3) Basal drag from a mantle plume; and 4) Backarc rifting. Each model was developed around different particular data, and all tend to perpetuate independently through selective data prioritisation. We present a new GPlates model, showing that the geological and geophysical correlations between the opposing SCS conjugate margins best agrees with a common initial development on the South China Margin, and that

regional development via protracted extension since the Mesozoic is in agreement with available paleomagnetic data for Borneo.The geodynamic mechanism for protracted lithospheric extension in SE Asia is via the development of progressive feedback processes, initiated by Mesozoic slab rollback and migration of the subduction zone beneath South China, leading to intracontinental thinning and extension. This in turn drove passive asthenospheric upwelling, increasing heat flow and crustal ductility, and enhancing further extension as a wide rift rather than narrow crustal neck. Subsequently, following sufficient continental extension, SCS oceanic spreading occurred. This feedback mechanism (involving shallow, not deep mantle processes) may enhance and enable intracontinental rifting elsewhere.

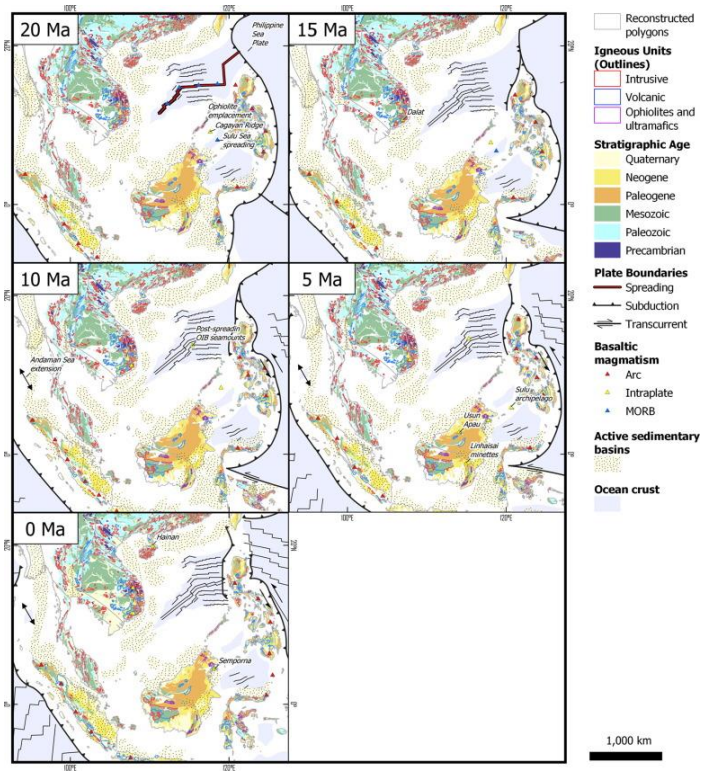

Figure 1. Proposed extensional Cenozoic history of SE Asia, highlighting key tectonic elements. Coastlines, isochrons, and plate boundaries adapted from Matthews et al., 2016, Hall, 2017, Hall, 2012, Hall, 2002, and Zahirovic et al. (2014). Sedimentary basins from Darman and Hasan Sidi, 2000, Pubellier and Morley, 2014, and Galin et al. (2017). Regional geology from Fig. 1. Regional basaltic magmatism from Fig. 5. Note that (as is typical in kinematic reconstructions) present-day coastlines are aids to geographic reference of past geological settings rather than implying the presence of similarly oriented past coastlines.

7. 米兰科维奇理论与季风

翻译人：杨会会 11849590@mail.sustech.edu.cn

Cheng H., Li H Y., Sha L J., et al. ***Milankovitch theory and monsoon*** *[J]. The Innovation, 2022.*

https://doi.org/10.1016/j.xinn.2022.100338

摘要：广为接受的“米兰科维奇理论”在轨道时间尺度上解释了日照引起的冰盖的增减及其对全球气候的影响。然而，在过去的半个世纪里，这个理论经常受到怀疑，特别是关于它的“100 ka 问题”。另一个缺点是“季风问题”，这个问题较少受到关注，但它与经典的米兰科维奇理论中没提到的季风动力学有关。季风盛行于覆盖半个地球表面的广大低纬度(~30°N - ~30°S)地区，并接收了大量太阳辐射，其动力系统不容忽视。本文综述了目前米兰科维奇理论存在的主要问题和研究前沿的进展。我们建议将重点从冰盖体积变化的最终结果转移到北半球高纬度日照变化与冰期终止事件（或冰盖融化速度）之间的因果关系上，以帮助解决经典的“100 ka 问题”。我们进一步讨论了与季风动力学特征有关的差异，特别是所谓的“海陆岁差相位悖论”和“中国 100 ka 问题”。我们认为这其中许多差异是表面的，可以通过应用整体的“季风系统科学”方法来解决。最后，我们建议将传统的 Kutzbach 轨道-季风假说与 Milankovitch 理论相结合，建立一个综合的“Milankovitch - Kutzbach 假说”，该假说可能解释冰盖和季风系统轨道水动力学的双重性，以及它们与北半球高纬度日照和热带间日照差的相互作用和各自的关系。

ABSTRACT: The widely accepted “Milankovitch Theory” explains insolation-induced waxing and waning of the ice sheets and their impact on the global climate on orbital-timescales. In the past half century, however, the theory has often come under scrutiny, especially regarding its “100-ka problem”. Another drawback, albeit the one that has received less attention, is the “monsoon problem”, which pertains to the exclusion of monsoon dynamics in classic Milankovitch Theory even though the monsoon prevails over the vast low-latitude (~30°N - ~30°S) region that covers half of the Earth’s surface and receives the bulk of solar radiation. In this review, we discuss the major issues with the current form of Milankovitch Theory and the progress made at the research

forefront. We suggest shifting the emphasis from the ultimate outcomes of the ice volume to the causal relationship between changes in northern high latitude insolation and ice age termination events (or ice sheet melting rate) to help reconcile the classic "100-ka problem". We further discuss the discrepancies associated with the characterization of monsoon dynamics, particularly the so-called "sea-land precession-phase paradox" and the "Chinese 100-ka problem". We suggest that many of these discrepancies are superficial, which can be resolved by applying a holistic "monsoon system science" approach. Finally, we propose blending the conventional Kutzbach Orbital-Monsoon Hypothesis, which calls for summer insolation forcing of monsoons, with Milankovitch Theory to formulate a combined "Milankovitch - Kutzbach Hypothesis" that can potentially explain the dual nature of orbital hydrodynamics of the ice sheet and monsoon systems, as well as their interplays and respective relationships with the northern high-latitude insolation and inter-tropical insolation differential.

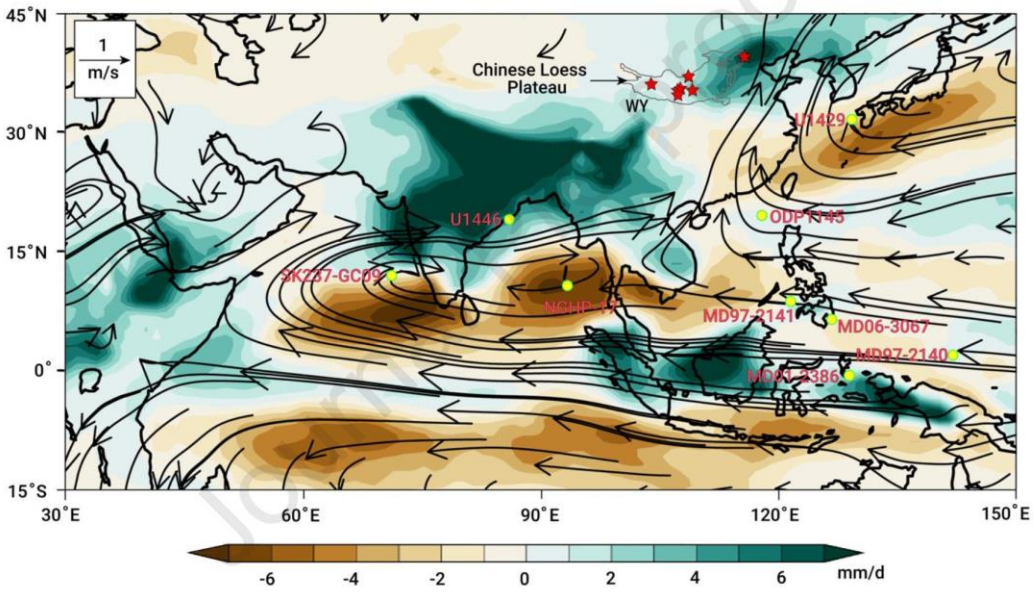

Figure 1. Simulated changes in precipitation rate (mm/d) and 850hPa wind vectors (m/s) over the AM and adjacent regions during boreal summer (JJA) between precession minimum (P_{min}) and maximum (P_{max}) from CESM experiments (modified from ref. 12). The gray line region depicts the Chinese Loess Plateau. Red asterisks indicate locations of loess-paleosol sections in the Chinese Loess Plateau (including Jingyuan, Yimaguan, Xifeng, Lingtai, Baoji, Luochuan and Jingbian

sections). Zhaitang section is at the NE plateau. White circles show marine core locations: MD97-2141, ODP1145, MD06- 3067, MD01-2386, U1429, and MD97-2140 in the western Pacific region, and SK237-GC09, U144622 and NGHP17in the Indian Ocean.

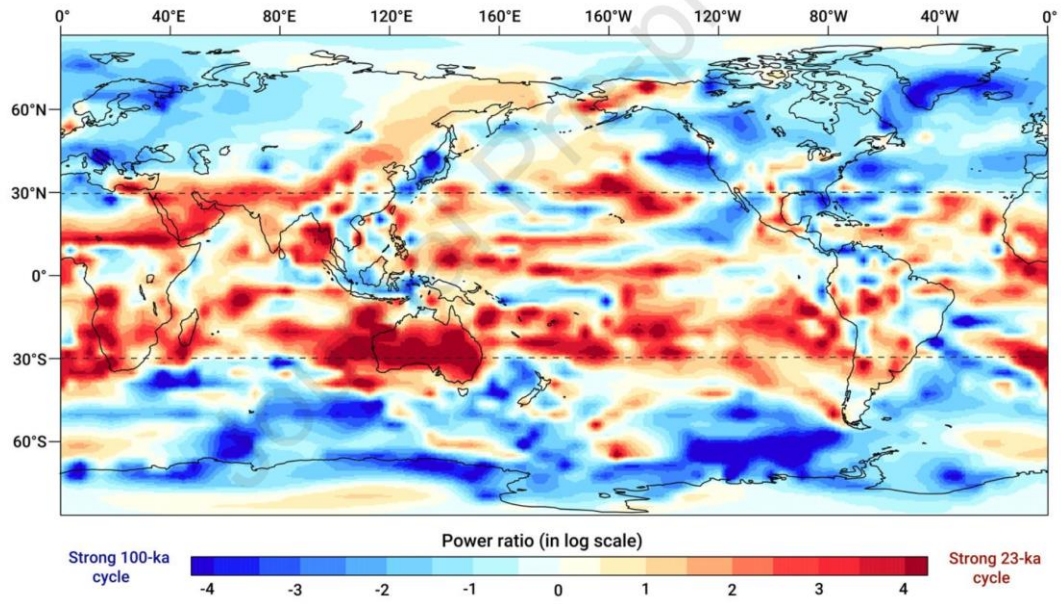

Figure 2. Simulated 23- and 100-ka cycle power ratios of annual precipitation illustrate the dual nature of global hydrodynamics in the high- and low-latitude regimes on orbital-scales Simulated cyclicality of annual precipitation variations for the past 300 ka. The transient simulations were initialized from the preindustrial conditions and forced by the orbital (ORB) and greenhouse gas (GHGs) forcings, as well as the prescribed fluctuations of continental ice sheets (ICE) for the past 300 ka.172 The simulated precipitation time series over each model grid cell was calculated to attain the power spectrum of annual precipitation for each grid cell, and the results are used to estimate the distribution of ~23-ka and ~100-ka band-average power. The natural log of this ratio was presented here so that the positive/negative values indicate that the 23-ka cycle of annual precipitation variabilities was stronger/weaker than the 100-ka cycle. The global annual precipitations show stronger ~23-ka cycles in low-latitude regions (~30°N-30°S as depicted by dashed-lines), in contrast to high-latitude regions where ~100-ka cycles are stronger.

8. 赤道印度洋碳酸盐埋藏的冰期-间冰期差异

翻译人：曹伟 11930854@qq.com

Yadav R., Naik S. ***Glacial interglacial differences in carbonate burial in the equatorial Indian Ocean*** *[J]. Geo-Marine Letters, 2022, 42, 12.*

https://doi.org/10.1007/s00367-022-00736-9

摘要：为了解过去 30 ka 碳酸盐埋藏的变化，我们利用来自大洋钻探计划 (ODP) 的岩心 Site716A（04.56° N, 73.17° E），取自 533 m 水深的马尔代夫（碳酸盐台地）海。我们分析了碳酸钙（$CaCO_3$%），沉积有机碳（C-org%），和选定浮游有孔虫种类（*Globigerinoides ruber*、*Pulleniatina obliquiloculata* 和 *Neogloboquadrina dutertrei*）的壳重，以了解末次冰期-全新世晚期碳酸盐保存的对比。我们的数据集显示，在末次盛冰期 (LGM) 和全新世期间，碳酸盐的保存量下降，这可能是由于沉积物中的有机物降解所致。LGM 期间 C-org/$CaCO_3$ 的比值相对高于末次冰消期（LDP）和全新世。此外，在 LDP 期间，浮游有孔虫壳重量较重表明碳酸盐保存相对增加，这与冰消期从海洋向大气释放的二氧化碳 (CO_2) 有关。

ABSTRACT: To understand the variations in carbonate burial for the last 30 kiloannum (ka), we have utilized a core from the Ocean Drilling Program (ODP), Site716A (04.56° N and 73.17° E) retrieved from a water depth of 533 m from the Maldives (carbonate platform) Sea. We analysed calcium carbonate ($CaCO_3$%), sedimentary organic carbon (C-org %) and shell weights of selected planktic foraminifera species (*Globigerinoides ruber, Pulleniatina obliquiloculata and Neogloboquadrina dutertrei*) to see the contrast in carbonate preservation during the late last glacial-Holocene. Our dataset reveals that carbonate preservation declined during the last glacial maximum (LGM) and the Holocene, probably due to organic matter degradation in sediments. The ratio of C-org/$CaCO_3$ was relatively higher during the LGM than during the last deglacial period (LDP) and the Holocene. Furthermore, the heavier planktic foraminifera shell weights during the LDP indicate relatively increased carbonate preservation, which is linked to the deglacial release of carbon

dioxide (CO_2) from the ocean to the atmosphere.

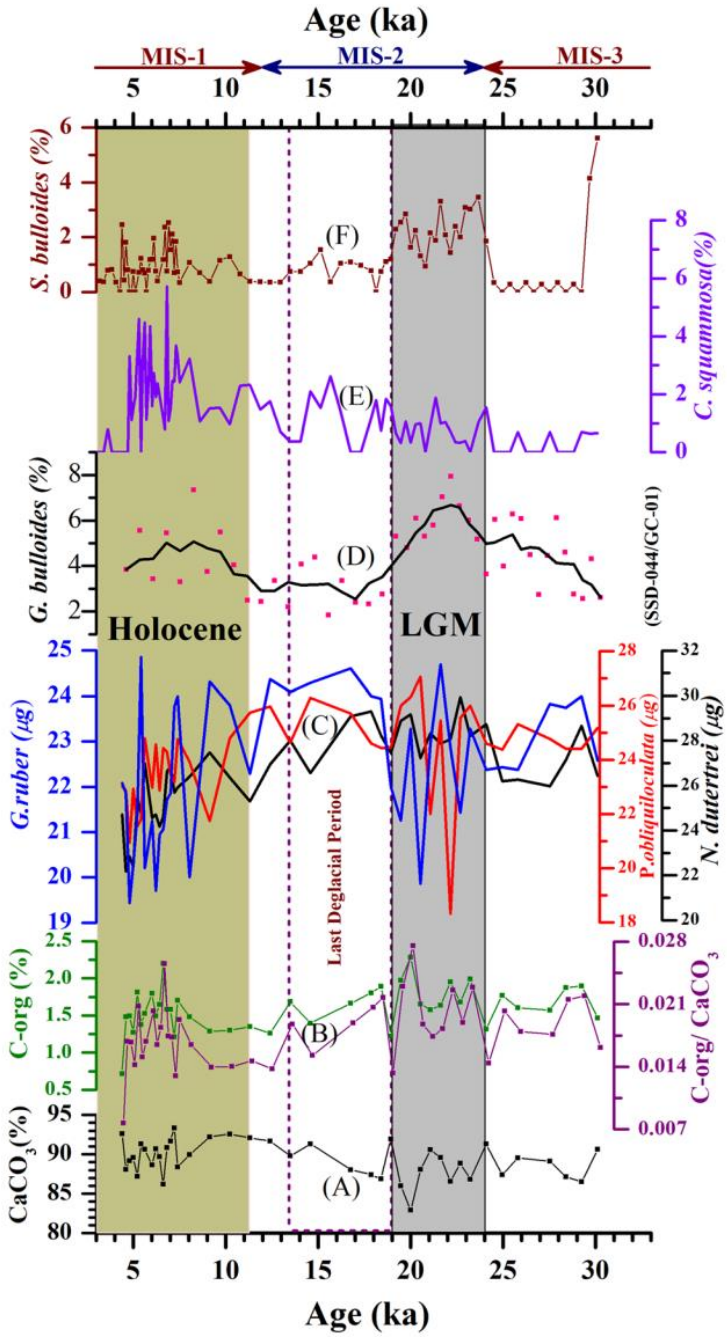

Figure 1. Down core variations of different proxies shown for the last 30 ka: **A** $CaCO_3$ percentage, **B** organic carbon (C-org) % and C-org/$CaCO_3$, **C** shell weights of *G. ruber, P. obliquiloculata* and *N. dutertrei*, **D** *G. bulloides* % (SSD-044/GC-01; Yadav et al. 2021), **E** *C. squammosa* (De et al. 2010) and **F** *S. bulloides* (De et al. 2010). The Last Glacial Maximum (LGM) and Holocene are marked by different shades, while the last deglacial is marked by dotted bars. The arrows indicate the marine isotopic stages (MIS-1, MIS-2 and MIS-3).

9. 磁场倒转速率模型及其对核幔边界热流变化的约束

翻译人：张伟杰 12031188@mail.sustech.edu.cn

Carbone V., Alberti T., Lepreti F., et al. ***A model for the geomagnetic field reversal rate and constraints on the heat flux variations at the core-mantle boundary*** *[J]. Scientific reports, 2020, 10(1): 1-9.*

https://doi.org/10.1038/s41598-020-69916-w

摘要：极性倒转是地磁发电机产生的磁场的一个显著特征。古地磁测量显示，在地球的历史中地球磁场极性经历了几百次的随机转换。极性倒转速率随时间的变化，可能遵循某种潜在的规律。虽然混沌动力系统可以描述地球磁极转换的短期行为，但对倒转速率的长期变化进行建模有些问题。因为它们发生在数千万年到数亿年的时间尺度上，与地幔对流时间尺度的量级相同。通过研究地磁倒转速率的数据，我们发现了具有可变频率的旋回的存在，并表明向数千万年不发生倒转时期(超时)的转变可以用二阶相变来描述，我们将其解释为由地核-地幔边界(CMB)的热通量变化所驱动。该模型使我们能够从倒转序列中提取出由 CMB 热流通量幅值变化引起的倒转速率敏感性的定量信息，从而提供有关地球深部内层的直接信息。

ABSTRACT: A striking feature of many natural magnetic fields generated by dynamo action is the occurrence of polarity reversals. Paleomagnetic measurements revealed that the Earth's magnetic field has been characterised by few hundred stochastic polarity switches during its history. The rate of reversals changes in time, maybe obeying some underlying regular pattern. While chaotic dynamical systems can describe the short-term behaviour of the switches of the Earth's magnetic polarity, modelling the long-term variations of the reversal rate is somewhat problematic, as they occur on timescales of tens to hundreds of millions of years, of the order of mantle convection timescales. By investigating data of geomagnetic reversal rates, we find the presence of cycles with variable frequency and show that the transition towards periods where reversals do not occur for tens of million years (superchrons) can be described by a second-order phase transition that we

interpret to be driven by variations of the heat flux at the core-mantle boundary (CMB). The model allows us to extract from the reversal sequence quantitative information on the susceptibility of the reversal rate caused by changes in the CMB heat flux amplitude, thus providing direct information on the deep inner layers of the Earth.

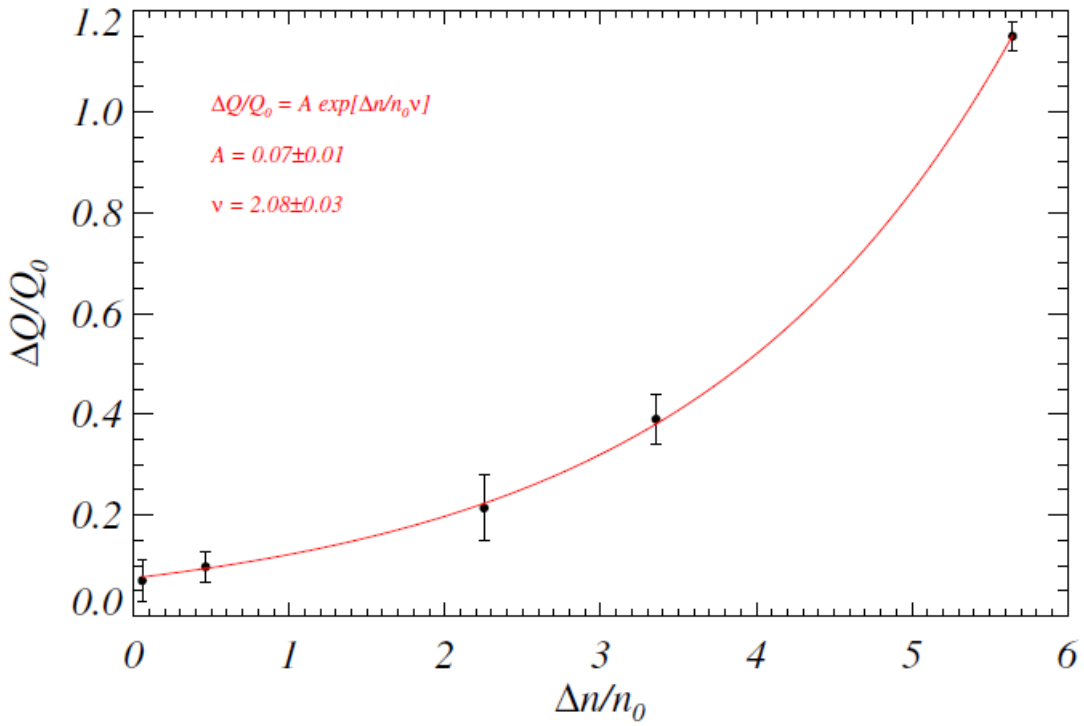

Figure 1. Estimated excess of CMB heat flow (black circles) as a function of the expected relative increase of reversals. The superposed red curve corresponds to an exponential function, obtained through a fit on the data, reported on the figure along with the best fit parameters.

10. 基于古地磁数据重建圣经中记录的战争

翻译人：李海 12031330@mail.sustech.edu.cn

Vaknin Y., Shaar R., Lipschits O., et al. ***Reconstructing Biblical Military Campaigns Using Geomagnetic Field Data*** *[J]. PNAS, 2022, 119(44), e2209117119.*

https://doi.org/10.1073/pnas.2209117119

摘要：希伯来圣经和其他古代中东的书籍记载了公元前 10 世纪至公元前 6 世纪期间，埃及人、亚兰人、亚述人和巴比伦人对黎凡特南部的军事行动。实际上，许多这一时期的破坏层已经在考古发掘中被识别出来。其中一些层位与特定的事件相关，被认为是准确的时间锚点。然而，其他破坏层的年代仍存在较大争议，对重建准确的军事行动影响较大，并提出了关于圣经记录的历史真实性的问题。本文，作者利用 20 个燃烧层和 2 个陶瓷中获得的古地磁方向及强度数据，并认为历史时期的时间锚点和其他破坏层及文物是同期的。在上述时期，该地区的地磁场异常变化，变化迅速，强度值高，峰值强度是现今的两倍多。这些数据对于确定这种短期变化很有帮助，它们解决了对抗以色列和犹大王国的战役、两个王国之间的关系及其政权的变化等问题。

ABSTRACT: The Hebrew Bible and other ancient Near Eastern texts describe Egyptian, Aramean, Assyrian, and Babylonian military campaigns to the Southern Levant during the 10th to sixth centuries BCE. Indeed, many destruction layers dated to this period have been unearthed in archaeological excavations. Several of these layers are securely linked to specific campaigns and are widely accepted as chronological anchors. However, the dating of many other destruction layers is often debated, challenging the ability to accurately reconstruct the different military campaigns and raising questions regarding the historicity of the biblical narrative. Here, we present a synchronization of the historically dated chronological anchors and other destruction layers and artifacts using the direction and/or intensity of the ancient geomagnetic field recorded in mud bricks from 20 burnt destruction layers and in two ceramic assemblages. During the period in question, the geomagnetic field in this region was extremely anomalous with rapid changes and high-intensity

values, including spikes of more than twice the intensity of today's field. The data are useful in the effort to pinpoint these short-term variations on the timescale, and they resolve chronological debates regarding the campaigns against the kingdoms of Israel and Judah, the relationship between the two kingdoms, and their administrations.

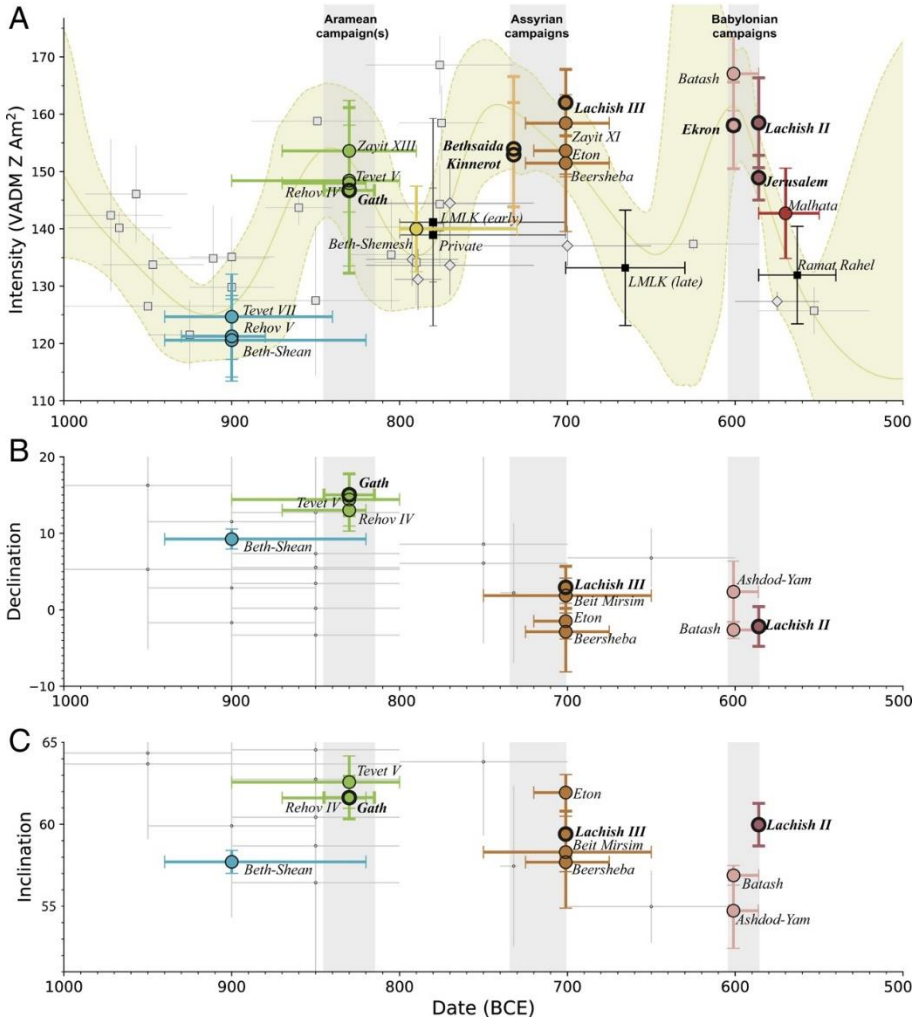

Figure 1. Archaeomagnetic results. (A) Field intensity results shown with LAC.v.1.0 (5) displayed as the virtual axial dipole moment (VADM). (B) The angle between the horizontal component and the geographic north (Declination). (C) The angle from the horizontal plane (Inclination). All directions are relocated to Jerusalem. Results from destruction layers are represented by colored circles (for color key, see Fig. 3). Note that some destruction layers have only intensity (A) or direction (B–C) results. Intensity results from pottery discussed in the text are represented by black squares. Intensity data included in LAC.v.1.0 (5) from Israel (squares) and Syria (diamonds) are

marked in gray. Previously published directions (3, 4) from the Levant are marked in gray dots. Chronological anchors are highlighted in bold. Note that the locations of the symbols on the time axis within the horizontal error bars were assigned arbitrarily, according to the different chronological considerations including the archaeomagnetic results. These assigned ages (SI Appendix, Tables S2–S6 and S9) are not considered as part of the prior data for the AH-RJMCMC model.

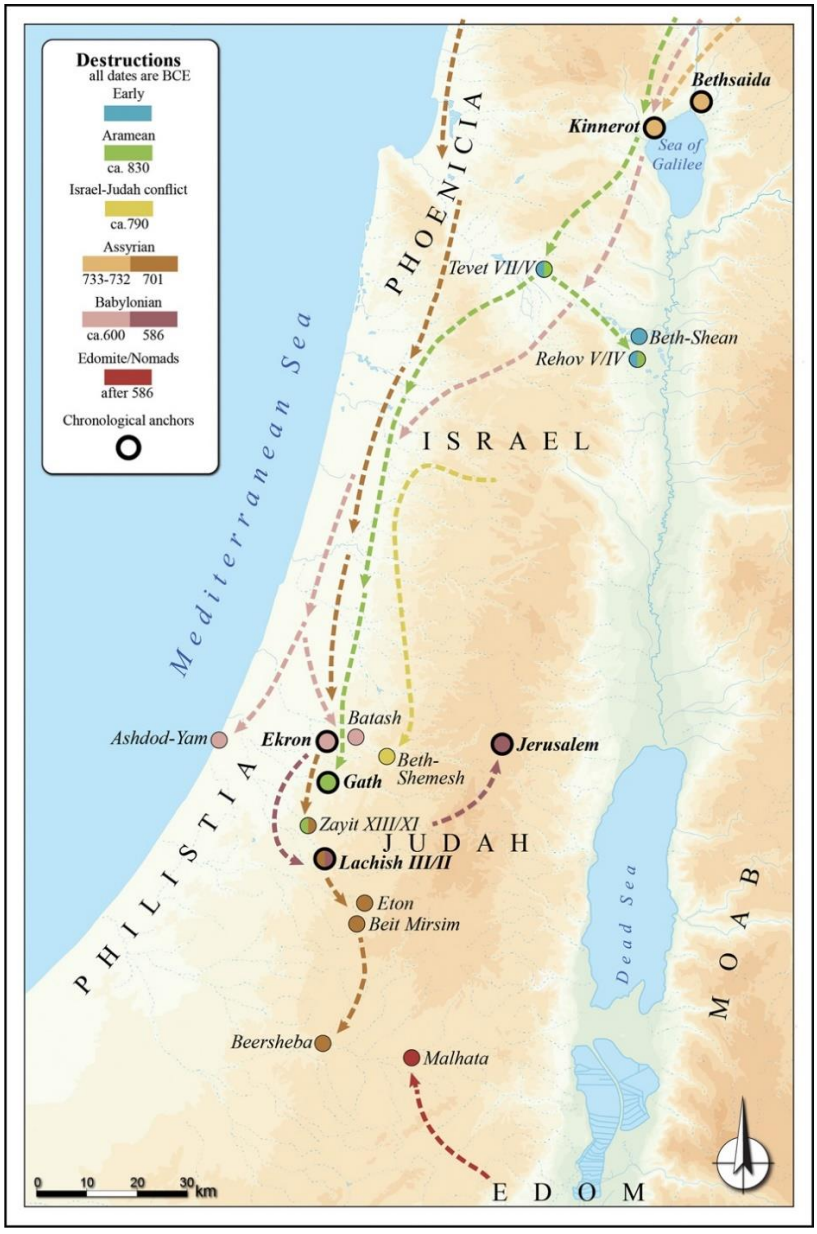

Figure 2. Map of the studied destruction layers and the different military campaigns. A schematic illustration of possible routes is presented following Rainey and Notley (21). Chronological anchors are highlighted in bold.

11. 科迪勒拉冰盖消退时期，由火山引发的海洋脱氧

翻译人：张亚南 zhangyn3@mail.sustech.edu.cn

Du J., Mix A C., Haley B A., et al. ***Volcanic trigger of ocean deoxygenation during Cordilleran ice sheet retreat*** *[J]. Nature, 2022, 611: 74-80.*

https://doi.org/10.1038/s41586-022-05267-y

摘要：北太平洋缺氧事件由于高生产力的影响，在末次冰消期以来持续了数千年，但触发机制及其与冰消期变暖的关系仍不确定。文中作者发现北太平洋最初的缺氧发生在科迪勒拉冰盖消退之后，与海洋沉积物中火山灰的增加有关。火山物质输入和 CIS 消退的时间先后关系表明区域火山活动爆发是由冰盖载荷减少引起的。作者假定 CIS 消退期间，火山灰的铁肥效应促进了铁限制海区的生产力，并使海洋系统朝着持续脱氧的方向发展。作者还发现过去约 5 万年中与 CIS 消退有关的缺氧事件。作者的发现表明，发生在短时间尺度上大气、海洋、冰冻圈和岩石圈系统显著的耦合过程，可能是海洋生物地球化学变化的重要驱动因素。

ABSTRACT: North Pacific deoxygenation events during the last deglaciation were sustained over millennia by high export productivity, but the triggering mechanisms and their links to deglacial warming remain uncertain. Here we find that initial deoxygenation in the North Pacific immediately after the Cordilleran ice sheet (CIS) retreat was associated with increased volcanic ash in seafloor sediments. Timing of volcanic inputs relative to CIS retreat suggests that regional explosive volcanism was initiated by ice unloading. We posit that iron fertilization by volcanic ash during CIS retreat fuelled ocean productivity in this otherwise iron-limited region, and tipped the marine system towards sustained deoxygenation. We also identify older deoxygenation events linked to CIS retreat over the past approximately 50,000 years (ref. 4). Our findings suggest that the apparent coupling between the atmosphere, ocean, cryosphere and solid-Earth systems occurs on relatively short timescales and can act as an important driver for ocean biogeochemical change.

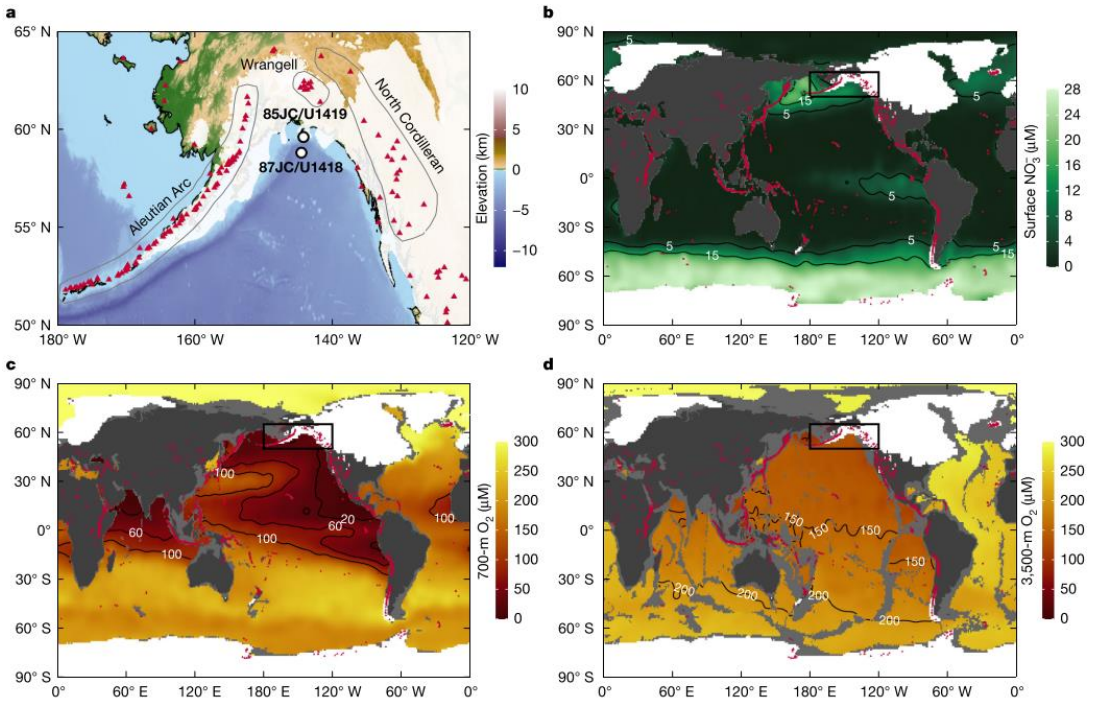

Figure 1. Geology and oceanography background. a, Modern land topography and ocean bathymetry in the Northeast Pacific. Circles mark the intermediatedepth site EW0408-85JC/IODP-U1419 and the abyssal site EW0408-87JC/IODPU1418. b, Modern global surface ocean nitrate concentration. c,d, Modern global ocean oxygen concentration at the 700-m (c) and 3,500-m (d) depths, respectively. In all panels, red triangles indicate Quaternary volcanoes. The three main regional volcanic fields adjacent to the Northeast Pacific are indicated in a. White fields show the LGM ice extent based on regional reconstruction (a) and the global ICE-7G model (b-d). The study region is indicated on the global maps by the black boxes.

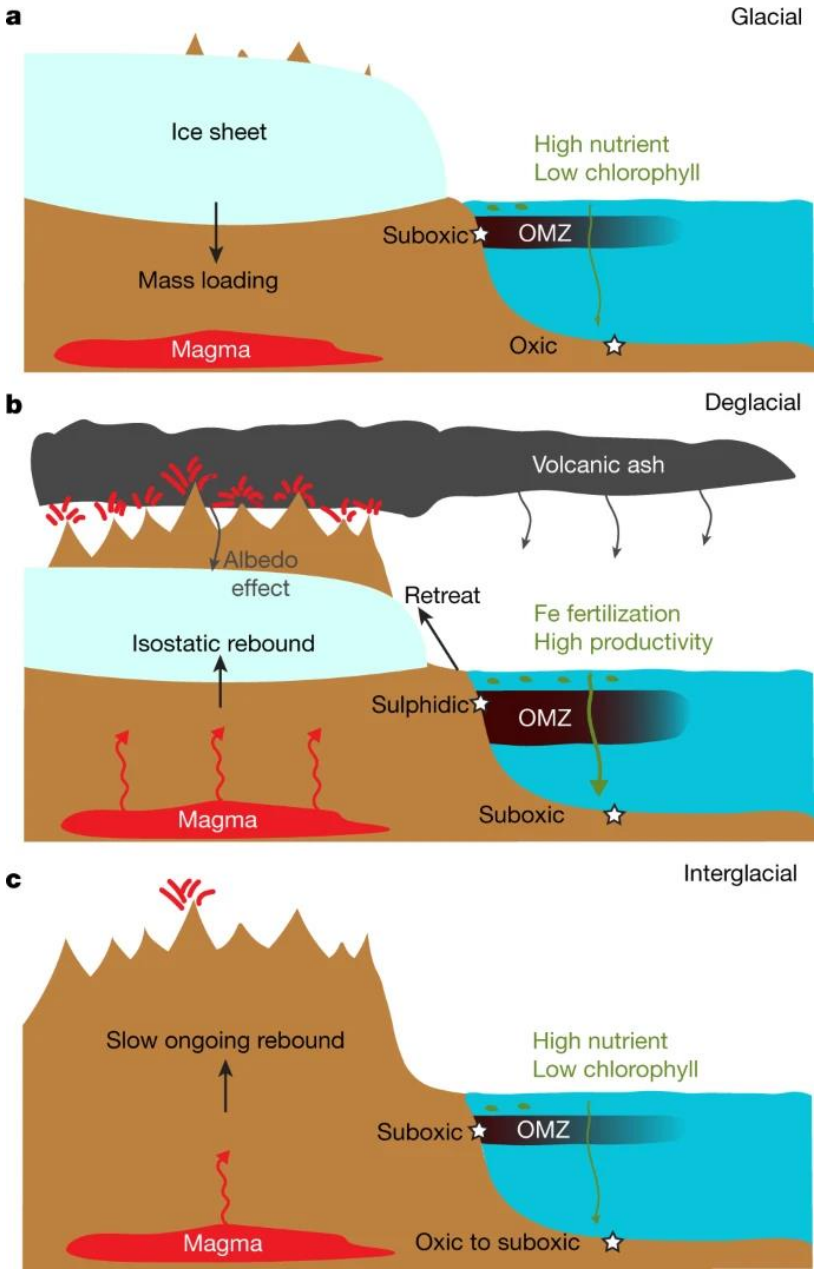

Figure 2. Proposed links between ice sheet retreat, volcanism and deoxygenation in the Northeast Pacific. a, The glacial state, with strong mass loading by the ice sheet. Volcanism is depressed. Seafloor oxygenation is similar or slightly better than today and surface productivity is similar or slightly weaker than today. b, The deglacial state, with increasing volcanism because of ice sheet retreat, which triggered high productivity and seafloor deoxygenation at both sites. The OMZ probably expanded but probably did not reach the abyssal site. The albedo effect of volcanic ash probably accelerated ice retreat. c, The interglacial state, after ice sheet retreat, volcanism becomes weaker. Surface productivity and seafloor oxygenation return to baseline conditions typical of the modern subpolar HNLC North Pacific. The stars mark the intermediate-depth and abyssal sites.

12. 过去 370 kyr 期间西赤道太平洋轨道尺度的温跃层温度变化

翻译人：夏文月 12231072@mail.sustech.edu.cn

Sagawa T., Okamura K., Murayama M. ***Orbital-scale thermocline temperature variability in the western equatorial Pacific during the last 370 kyr*** *[J]. Palaeogeography, Palaeoclimatology, Palaeoecology, 2022, 608, 111285.*

https://doi.org/10.1016/j.palaeo.2022.111285

摘要：热带次表层环流在调节两半球之间的热量和盐分运输以及海洋-大气的相互作用中起着关键作用（例如，厄尔尼诺-南方涛动；ENSO）。因此，了解过去热带温跃层的行为对于预测长期的全球气候变化非常重要。在此，基于从西赤道太平洋（WEP）的沉积物芯中获取的近 370 kyr 浮游有孔虫斜室普林虫的 Mg/Ca 测量数据，我们提供了轨道尺度温跃层的温度（TT）记录。WEP 海表温和温跃层温度（TT）之间的垂直温度梯度与热带太平洋区域 SST 梯度的长期趋势和斜率信号显示出弱的正相关性。这两个梯度的关系与现代 ENSO 的变化不一致，表明长期 TT 变化主要取决于另一种机制。频谱分析显示，TT 变化存在较强的斜率和岁差信号。由于本地日照量的斜率信号非常弱，TT 变率中显著的斜率信号意味着热带温跃层环流受温带外影响。因此，我们的研究结果表明，连接着热带地区和热带以外地区的地下环流在轨道尺度的热带温跃层变率上起着重要的作用。

ABSTRACT: Tropical subsurface circulation plays a key role in regulating heat and salt transport between the hemispheres, and in ocean–atmosphere interactions (e.g., El Ni˜no-Southern Oscillation; ENSO). Therefore, understanding the past behavior of tropical thermoclines is important for predicting long-term global climate change. Here, we provide an orbital-scale thermocline temperature (TT) record based on Mg/Ca measurements of planktonic foraminifer Pulleniatina obliquiloculata in sediment cores obtained from the western equatorial Pacific (WEP) for the last 370 kyr. The vertical temperature gradient between sea surface temperature (SST) and TT in WEP showed weak positive correlations with the tropical Pacific zonal SST gradient in long-term trend

and obliquity signal. The relationship of the two gradients does not coincide with modern ENSO variability, suggesting that the long-term TT variation depend primarily on another mechanism. Spectral analysis indicated that TT variability has strong signals in both the obliquity and precession bands. Since the obliquity signal is very weak in local insolation, the significant obliquity in TT variability implies an extratropical influence on tropical thermocline circulation. Therefore, our findings suggest that the subsurface circulation connecting the tropics and extra-tropics plays an essential role in orbital-scale tropical thermocline variability.

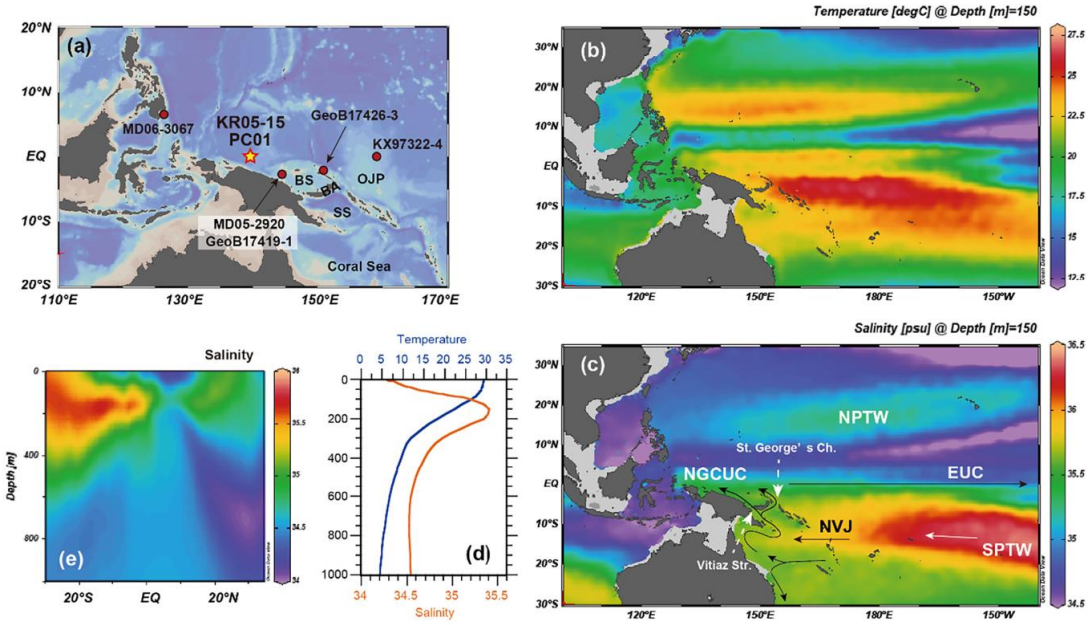

Figure 1. (a) Map showing the sites investigated in this study and reference sites. Annual mean temperature (b) and salinity (c) at 150-m depth [World Ocean Atlas 2018 (Locarnini et al., 2018; Zweng et al., 2018)]. Arrows in (c) indicate subsurface circulation. (d) Vertical profiles of temperature and salinity at the study site. (e) Latitudinal section of salinity along 155◦E. BA: Bismarck Archipelago, BS: Bismarck Sea, EUC: Equatorial Undercurrent, NGCUC: New Guinea Coastal Undercurrent, NPTW: North Pacific Tropical Water, NVJ: North Vanuatu Jet, OJP: Ontong Java Plateau, SPTW: South Pacific Tropical Water, SS: Solomon Sea.

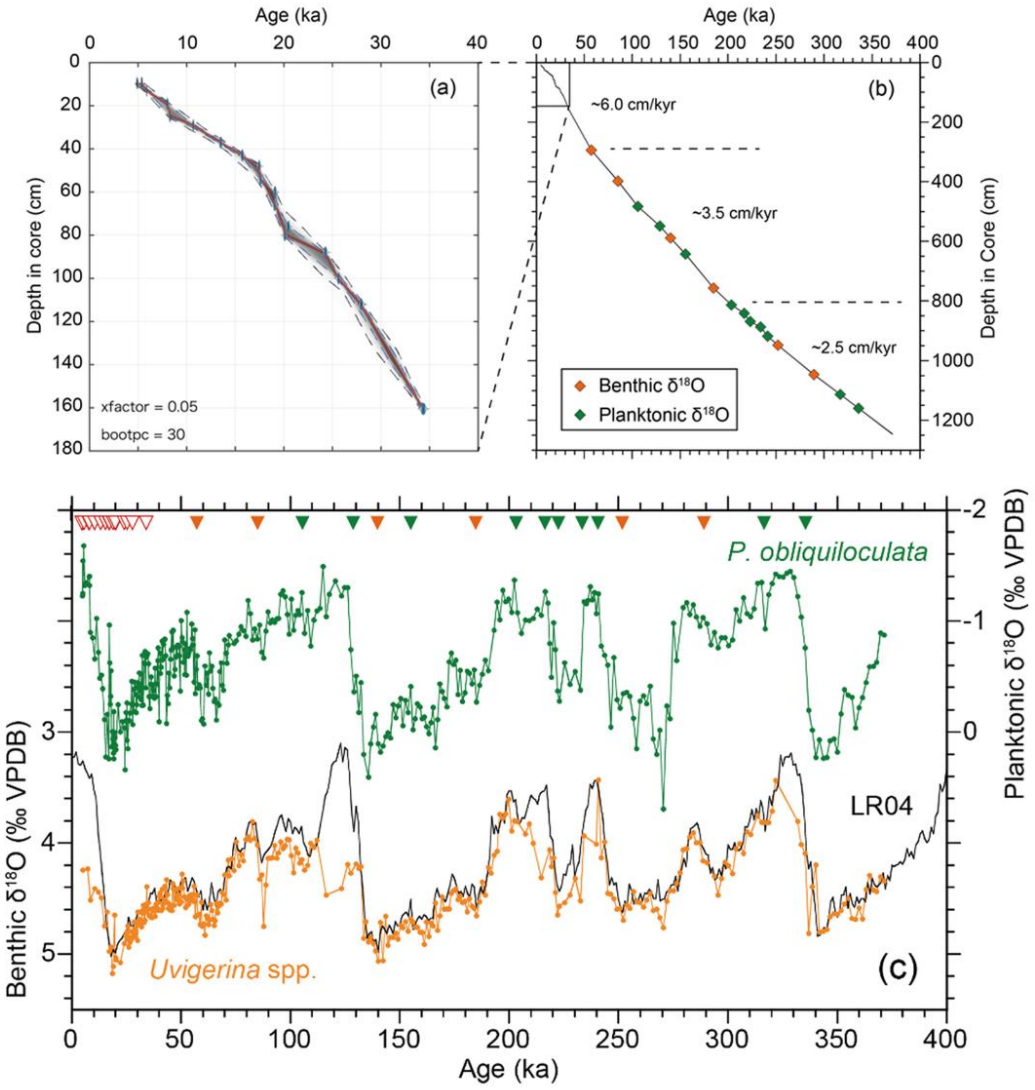

Figure 2. Age–depth relationship of KR05–15 PC01 for the upper interval based on accelerator mass spectrometry radiocarbon analysis (a), and for the lower interval based on isotope stratigraphy (b). (c) Comparison of oxygen isotopes of PC01, P. obliquiloculata (green) and Uvigerina spp. (orange), with the LR04 isotope stack (black line; Lisicki and Raymo, 2005). Triangles on the top horizontal axis represent age control points based on radiocarbon (red), benthic δ18O (orange), and planktonic δ18O (green) data. The LR04 stack curve is also shown for comparison. (For interpretation of the references to colour in this figure legend, the reader is referred to the web version of this article.)

13. 跨南极山脉 60Ma 以来的冰川作用

翻译人：刘宇星 liuyx2018@mail.sustech.edu.cn

Barr I D., Spagnolo M., Rea B R., et al. ***60 million years of glaciation in the Transantarctic Mountains*** *[J]. Nature Communications, 2022, 13(1): 1-7.*

https://doi.org/10.1038/s41467-022-33310-z

摘要：距今约 83 Ma 时南极大陆到达了其今天的极地位置，并在约 34Ma 时被冰盖所笼罩，这与始新世-渐新世交界的急剧全球变冷相吻合。然而，目前尚不清楚第一批南极冰川是在此之前形成的，还是更早就出现的。这里我们表明，在古新世晚期（约 60-56 Ma）和始新世中期（约 48-40 Ma），跨南极山脉可能存在山地冰川。温带（暖基）冰川在始新世晚期（约 40-34 Ma）盛行，并且在渐新世（约 34-23 Ma）期间数量减少，之后是更大的、可能基于冷基的冰块（包括冰盖）占主导地位。在中新世气候适宜期（~15 Ma）期间，一些温带山地冰川存在，然后广泛转向冷基的冰川。我们的发现强调了南极洲冰川作用的长期性，并表明即使在新生代早期的温室世界中也存在冰川。

ABSTRACT: The Antarctic continent reached its current polar location ~83 Ma and became shrouded by ice sheets ~34 Ma, coincident with dramatic global cooling at the Eocene-Oligocene boundary. However, it is not known whether the first Antarctic glaciers formed immediately prior to this or were present significantly earlier. Here we show that mountain glaciers were likely present in the Transantarctic Mountains during the Late Palaeocene (~60–56 Ma) and middle Eocene (~48–40 Ma). Temperate (warm-based) glaciers were prevalent during the Late Eocene (~40–34 Ma) and, in reduced numbers, during the Oligocene (~34–23 Ma), before larger, likely cold-based, ice masses (including ice sheets) dominated. Some temperate mountain glaciers were present during the Miocene Climatic Optimum (~15 Ma), before a widespread switch to cold-based glaciation. Our findings highlight the longevity of glaciation in Antarctica and suggest that glaciers were present even during the Early-Cenozoic greenhouse world.

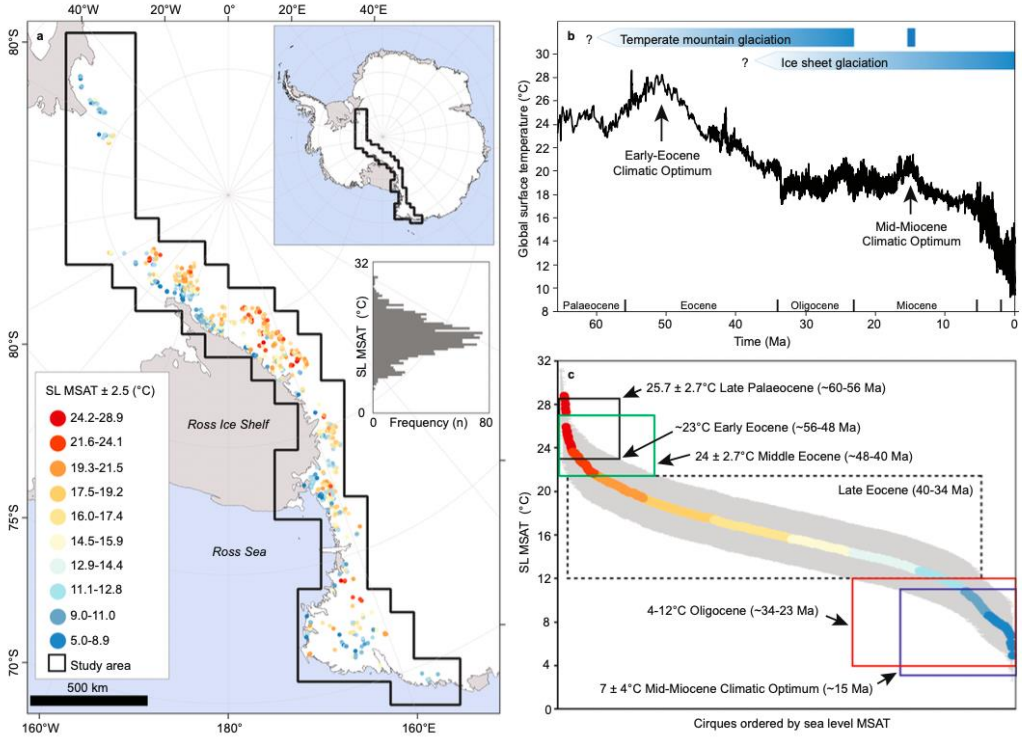

Figure 1. Palaeotemperature reconstructions from Antarctica and globally. a. Glacier-free cirques (n = 1292) in the Transantarctic Mountains colored according to the sea level mean summer air temperature (SL MSAT) required for them to be occupied by temperate (warm-based) mountain glaciers. The inset histogram shows the frequency distribution of SL MSAT. Antarctic coastline data from the SCAR Antarctic Digital Database, accessed [2021] license: https://creativecommons.org/licenses/by/4.0/ . b. Global surface temperature data for the Cenozoic4, highlighting key climatic periods referred to in the text, and our interpretation of the glacial history of the TAM. c. Cirques ordered by SL MSAT (grey area represents the ±2.5 °C MSAT uncertainty) required for them to be occupied by temperate mountain glaciers. Colors are based on the values in subplot (a). Antarctic temperature estimates for different time periods in subplot (c) are based on published data from biological proxies (Supplementary Table 1).

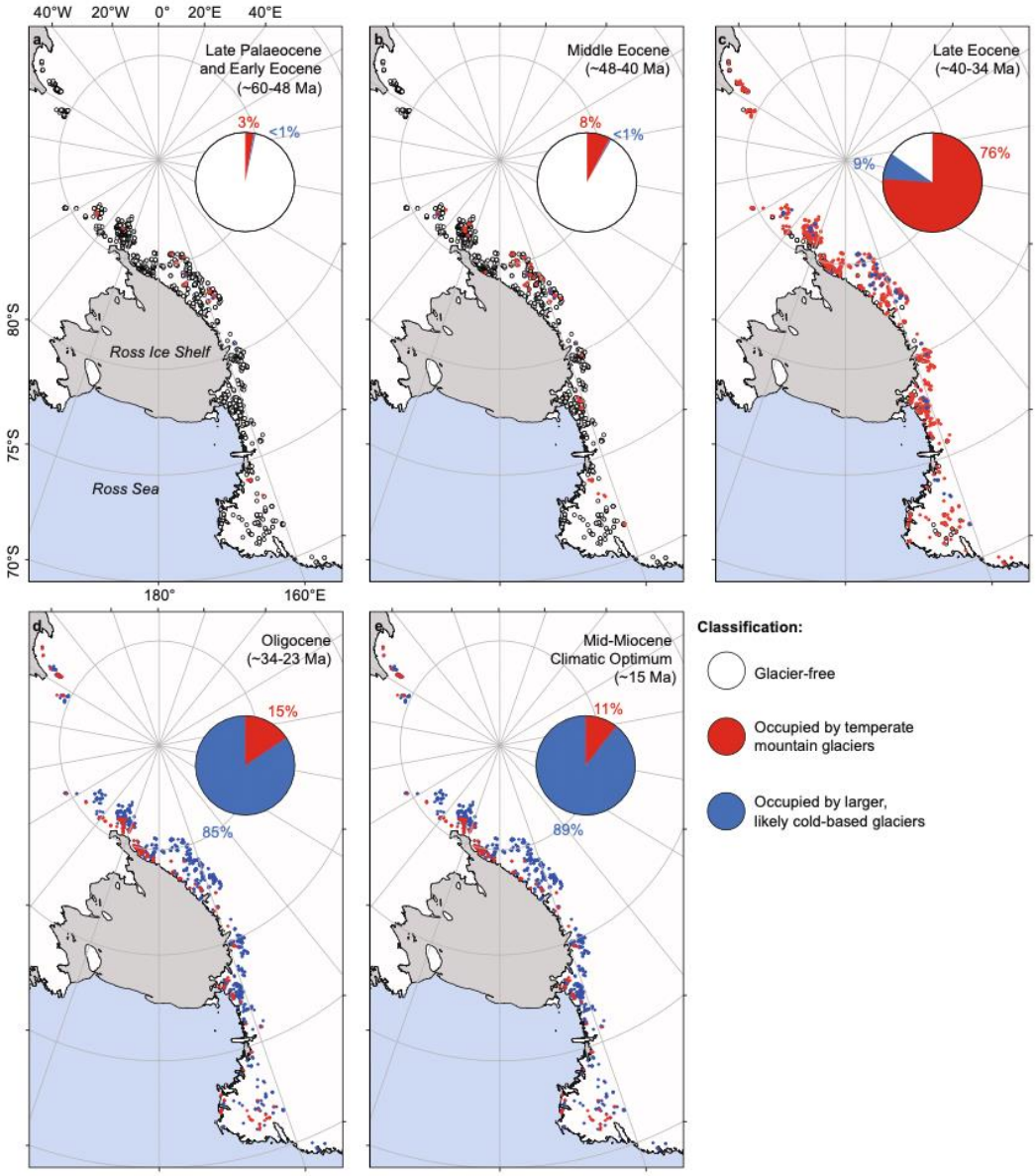

Figure 2. Glacier-free cirques in the Transantarctic Mountains are classified according to their glacial status during various periods of the Cenozoic. a–e. Pie charts show the percentage of cirques classified as glacier free (white), occupied by temperate mountain glaciers (red %), and occupied by larger, likely cold-based glaciers (blue %) for the total population (n = 1292). Antarctic coastline data from the SCAR Antarctic Digital Database, accessed [2021] license: https://creativecommons.org/licenses/by/4.0/ .

14. 自 1880 年以来东亚冬季温度的多年变化:内部变化与外部强迫

翻译人：聂美娟 12232216@mail.sustech.edu.cn

Miao J., Jiang D., et al. ***Multidecadal variations in East Asian winter temperature since 1880: Internal variability versus external forcing*** *[J]. Geophysical Research Letters, 49, e2022GL099597.*

https://doi.org/10.1029/2022GL099597

摘要：本研究通过分析三个观测数据集和 12 个耦合模式的大型集成模拟，探讨了 1880 年以来东亚冬季(12 月-2 月)平均气温(EASAT)的多年变化中内部变化和外部强迫的相对贡献。结果表明，内部变化在东亚海温多年变化中起主导作用。具体而言，大西洋多年代际振荡(AMO)通过欧亚大陆的大气遥相关从而影响 EASAT，内部产生的 EASAT 变化与 AMO 指数之间的相关系数为−0.49。相比之下，由于外部强迫因子的抵消作用，外部强迫仅调节了观测到的 EASAT 变化。换而言之，温室气体浓度的多年变化和人为/火山气溶胶的贡献分别为正贡献和负贡献。由于 AMO 和人为强迫的可预测性，我们的新发现有助于对未来几十年的 EASAT 进行预测。

ABSTRACT: This study investigates the relative contributions of internal variability and external forcing to multidecadal variations in the winter (December-February) East Asian averaged surface air temperature (EASAT) since 1880 by analyzing three observational datasets and large ensemble simulations from 12 coupled models. The results indicate that the internal variability plays a dominant role in the EASAT multidecadal variations. Specifically, the Atlantic Multidecadal Oscillation (AMO) affects the EASAT via an atmospheric teleconnection across the Eurasian continent, and the correlation coefficient between internally generated EASAT variation and the AMO index is −0.49. In comparison, the external forcings only modulate the observed EASAT variations due to offsetting effects of the external forcing agents. That is, the multidecadal variations in the greenhouse gas concentrations and anthropogenic/volcanic aerosols make positive and

negative contributions, respectively. Our new finding is conducive to EASAT predictions in the following decades due to the predictability of AMO and anthropogenic forcings.

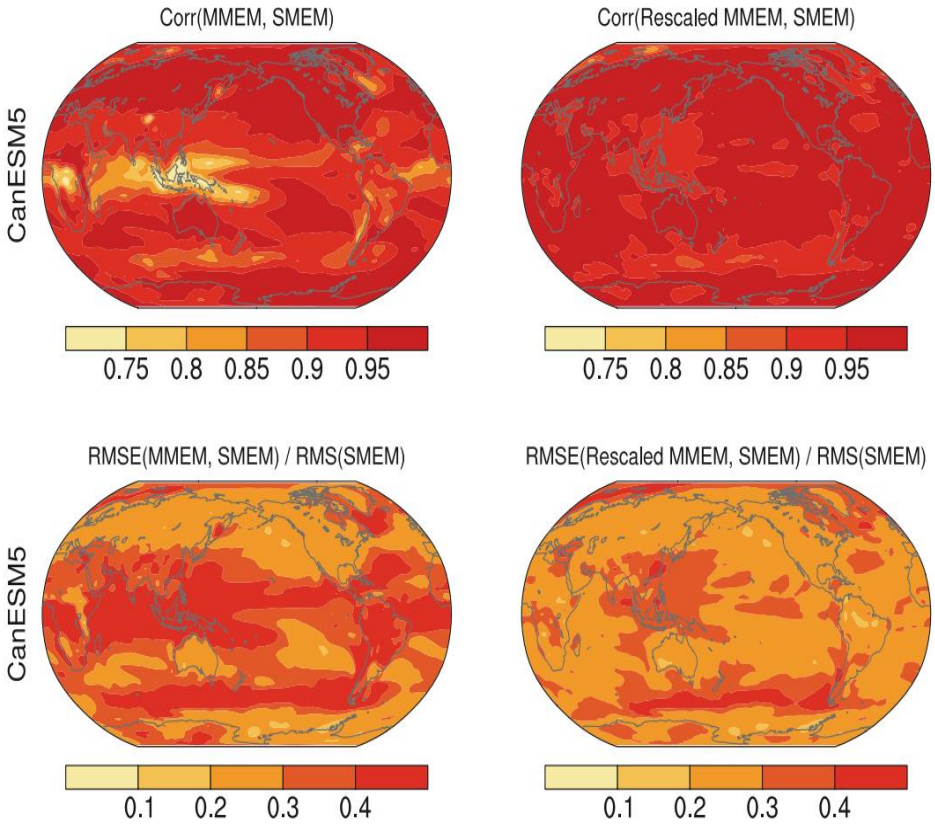

Figure 1. (top) Correlation coefficients for the period 1880–2013 between the internal components of raw winter surface air temperature estimated with the single-model ensemble mean (SMEM) and those with the (left) 12-model multimodel ensemble mean (MMEM) or (right) rescaled 12-model MMEM in the first realization of CanESM5 Large Ensemble. (bottom) As in (top) but for root-mean-square differences relative to root-mean-square of the internal components estimated with the SMEM.

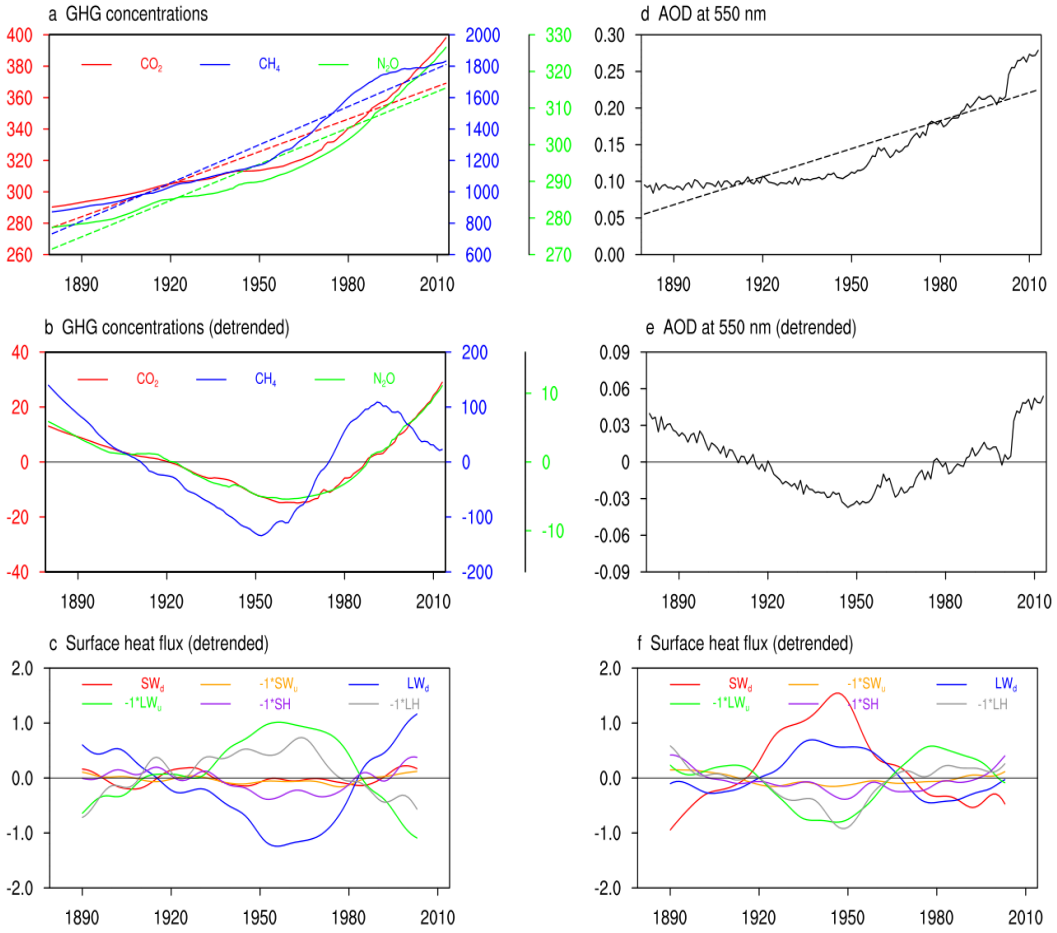

Figure 2. (a) Time series of the raw global mean concentrations of the three most important well-mixed greenhouse gases (solid line) in Northern Hemisphere winter for the period 1880–2013, including CO_2 (units: ppm), CH_4 and N_2O (units: ppb). The linear trends are overlaid as dashed lines. (b) As in (a) but for the detrended time series. (c) Detrended and 21-year low-pass filtered time series of East Asian averaged winter mean surface heat fluxes (units: W m^{-2}) in the multimodel ensemble mean (MMEM) greenhouse gas-forced simulations, including downward shortwave flux (SW_d), upward shortwave flux (SW_u; multiplied by negative one), downward longwave flux (LW_d), upward longwave flux (LW_u; multiplied by negative one), sensible heat flux (SH; multiplied by negative one), and latent heat flux (LH; multiplied by negative one). (d) Time series of the raw East Asian averaged winter mean tropospheric aerosol optical depth at 550 nm (solid line) in the MMEM anthropogenic aerosol-forced simulations for the period 1880–2013, with linear trends overlaid as dashed lines. (e) As in (d) but for the detrended time series. (f) As in (c) but in the MMEM anthropogenic aerosol-forced simulations.